Doctoral Dissertation
博士論文

Development and demonstration of label-free multiphoton imaging flow cytometry
(ラベルフリー多光子イメージングフローサイトメトリーの開発と実証)

A Dissertation Submitted for the Degree of Doctor of Philosophy
September 2023
令和 5 年 9 月博士（理学）申請

Department of Chemistry, Graduate School of Science,
The University of Tokyo
東京大学大学院理学系研究科化学専攻

Ryo Kinegawa
木下川　涼

Abstract

Development and demonstration of label-free multiphoton imaging flow cytometry

Ryo Kinegawa

Introduction

Flow cytometry is a powerful technique to analyze and sort single cells and particles in heterogeneous mixtures at high throughput. By incorporating principles of fluid dynamics, optics, electronics, and data analysis, flow cytometry provides detailed information in a rapid manner. Because of its splendid utility, flow cytometry is widely used in various fields such as immunology, microbiology, molecular biology. Conventional flow cytometry such as fluorescence-activated cell sorting (FACS) [1] is capable of high-throughput measurement of fluorescence signals from cells. However, it lacks spatial information in exchange for its high throughput, missing the cell morphology and biomarker distribution. Fluorescence imaging flow cytometry has both the advantages of flow cytometry and imaging capabilities, enabling high-throughput morphological information measurements. In spite of its great capabilities of identification and classification of individual single cells based on captured fluorescence images as described in the last section, fluorescence imaging flow cytometry remains drawbacks due to its labeling, such as cytotoxicity and its non-specific binding.

Label-free imaging flow cytometry is emerging as a valuable tool for research in biology and life science, overcoming technical constraints in traditional fluorescence-based imaging flow cytometry mentioned above. Until now, mainly two different types of label-free imaging flow cytometry have been demonstrated in addition to conventional bright-field imaging flow cytometry. First, optofluidic time-stretch flow cytometry was developed for quantitative phase imaging [2]. It captures quantitative phase images of large numbers of single cells at high event rates of over 10,000 events per second. Optofluidic time-stretch quantitative phase imaging flow cytometry enabled large-scale screening of single cells using computational approaches such as compressive sensing and machine learning. Next, vibrational imaging flow cytometry via stimulated Raman scattering (SRS) was developed [3]. SRS imaging flow cytometry provided chemical images of intercellular molecules based on their Raman signal intensities with a throughput of up to 140 eps. This technique enabled visualization of intercellular contrast of lipid, paramylon, and chlorophyll in *E. gracillis* cells, letting a classification of the cells cultured under different conditions with an accuracy of > 99 %. Even with the progress of optofluidic time-stretch imaging flow cytometry and SRS imaging flow cytometry, the entire characterization of a broad range of complex biological systems in a label-free way remains challenging because of the limited information acquired by these methods. Especially optofluidic quantitative time-stretch phase imaging lacks the ability to provide chemical specificity, thus failing to assess the chemical composition of cells while providing three-dimensional morphological details of single cells. Conversely, SRS imaging flow cytometry provides chemical specificity, but its chemical imaging capabilities are limited by small Raman scattering cross-sections of biomolecules (10-30 cm^2/sr) and the narrow bandwidth of SRS (typically limited to a high wavenumber range from 2,800 to 3,200 cm^{-1}), which stems from the scarcity of available laser sources. Even though the fusion of label-free imaging and machine learning has certainly advanced the biological understanding extracted from the collected images, accessing more chemical details at the raw data level is vital for leveraging the full potential of label-free imaging flow cytometry. Especially, it is still challenging to carry out imaging of some key biomolecules, such as starch and collagen, by label-free imaging flow cytometry.

In this thesis, I developed a new variety of label-free imaging flow cytometry for high-throughput visualization of starch and collagen in living cells: label-free multiphoton imaging flow cytometry [4]. My multiphoton imaging flow cytometer provides nonlinear optical images, where image contrast is produced by two kinds of nonlinear optical effects: second-harmonic generation (SHG) and four-wave mixing (FWM). SHG is an optical effect resulting from the second-order optical susceptibility of materials and is employed to visualize starch, collagen, and other non-centrosymmetric materials. On the other hand, four-wave mixing (FWM) is a third-order

nonlinear optical process that occurs under the presence of intense light and involves the interaction of three initial light waves with samples, resulting in the generation of a fourth wavelength. Notably, FWM has been utilized for high-contrast label-free visualization of cytoplasm within cell. The multiphoton imaging flow cytometer consists of a microfluidic system, a dual color (SHG and FWM) microscope with a 2D-scanned focused beam, and a fast signal acquisition circuit designed to simultaneously capture SHG and FWM images of flowing cells. Consequently, the multiphoton imaging flow cytometer can acquire SHG and FWM images with a pixel resolution of 100 × 100 pixels, a spatial resolution of 500 nm, a field of view of 50 μm × 50 μm, and an intensity depth of 14-bit at a high event rate of 4-5 event per second.

Multiphoton imaging flow cytometer

The schematic of my label-free multiphoton imaging flow cytometer is depicted as Fig. 1. In the flow cytometer, in the beginning, cultured cells are transferred from Petri dishes to syringes. Then, these cells in syringes are delivered into a microfluidic chip (SC-BU-300300-L, Translume) by a syringe pump (Pump 11 Elite, Harvard Apparatus). The flow speed of cells is controlled as 2 mm/s by the pump. Flowing cells in the microfluidic chip are centrally focused into a single line by acoustic focusing with a piezoelectric element (2.44Z25*30R-SYX(C-213), Nihon Denkei Co., Ltd.), which is attached on the rear side of the microfluidic chip. At the moment that each cell goes through a focused beam spot of HeNe laser (HNL020LB, Thorlabs), a change in the direction of the forward-scattered beam is registered by a Si avalanche photodetector (APD120A/M, Thorlabs), triggering multiphoton imaging (SHG and FWM imaging). Flowing cells then arrive at the SHG and FWM imaging section. A Ti:sapphire laser (Synergy, Spectra Physics) with a FWHM of temporal pulse duration of 17 fs, a repetition rate of 75 MHz, a central wavelength of 793 nm, and a FWHM of spectral bandwidth of 43 nm. A 2D-galvanometric scanner (6210H, Cambridge Technology) is controlled by a triangle wave at 5 Hz (slow axis) and another triangle wave at 500 Hz (fast axis) so that the incident laser beam is scanned over 150 μm in 100 ms (along the stream direction) and 50 μm at 5 Hz (perpendicular to the stream direction) on the focal plane. For the separation of the SHG signal from others, three band-pass filters (FBH400-40, Thorlabs) with a center wavelength of 400 nm and a FWHM of bandwidth of 40 nm. Then, the SHG signal is detected by a photomultiplier tube (H7732-01, Hamamatsu Photonics) with a high quantum efficiency. Fig. 2 (a) and (b) show examples of constructed FWM and SHG images of *Chromochloris zofingiensis* cells, respectively. The FWM image visualizes the morphology of the cell based on the third-order susceptibility of molecules within the cells. On the other hand, the SHG image selectively visualizes the distribution of starch accumulated in the cells. Fig. 2 (c) is the composite image of Fig. 2 (a) and (b).

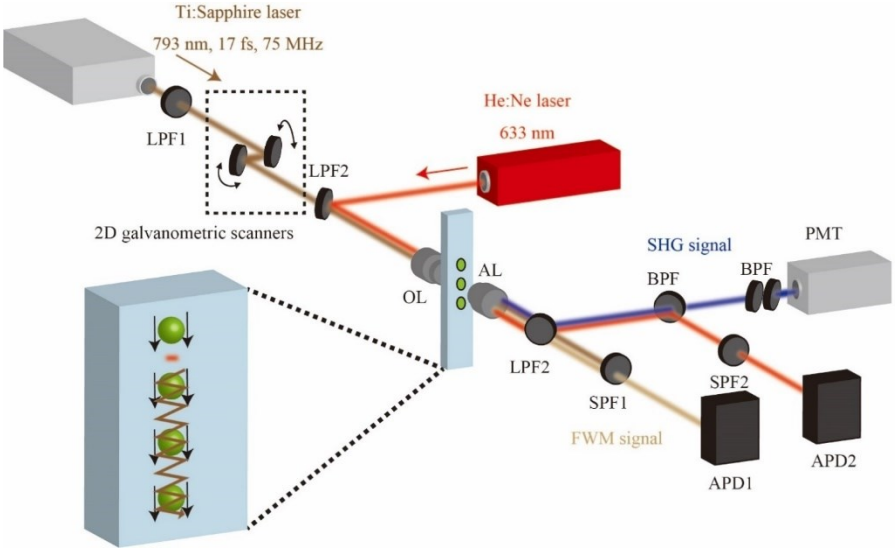

Fig. 1. Schematic of FWM and SHG imaging flow cytometer. APD1: avalanche photodetector for FWM signal detection; APD2: avalanche photodetector for He:Ne laser beam detection; PMT: photomultiplier tube; LPF1: 750-nm long-pass filter; LPF2: 650-nm long-pass filter; SPF1: 750-nm short-pass filter; SPF2: 700-nm short-pass filter; BPF: 400-nm bandpass filter; OL: objective lens; AL: achromatic lens.

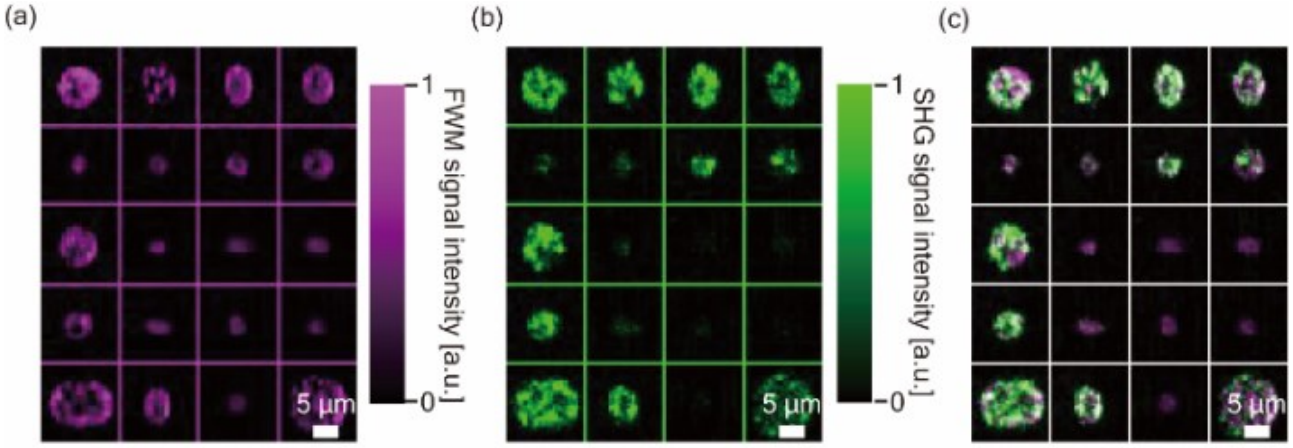

Fig. 2. FWM and SHG images taken by the label-free multiphoton imaging flow cytometer. (a) and (b) are constructed FWM and SHG images of *C. zofingiensis* cells, correspondingly. (c) composite image of FWM and SHG images.

Results of multiphoton imaging flow cytometry

To demonstrate the utility of multiphoton imaging flow cytometry, I carried out multiphoton imaging of the *C. zofingiensis* cells from day 0 to day 9 after the glucose supplementation with a laser power of 70 mW on the sample and a pixel duration of 10 µs (equivalent to an image capture duration of 100 ms) with the label-free imaging flow cytometer. I obtained 2,000 FWM and SHG images of *C. zofingiensis* cells for each cultural condition. Violin plots of the *C. zofingiensis* cell's area are shown in Fig. 3. It is indicated that the cell size reached a maximum at around day 6 and then reduced.

To better understand the morphogenesis of *C. zofingiensis,* I performed the FWM and SHG image analysis to see how the spatial distribution of starch accumulated in *C. zofingiensis* cells changes after glucose supplementation. The scatter plots of "the fraction of SHG intensity" and the *C. zofingiensis* cell size in Fig. 4. "The fraction of SHG intensity" was computed by using the "MeasureObjectIntensityDistribution" module on *CellProfiler 4.1.3*. As a first step in this process, Each *C. zofingiensis* cell visualized by FWM imaging was split into the inner bin (bin 1) and the outer bin (bin 2). Next, the sum of SHG signal intensities in each bin was computed to derive "the fraction of SHG intensity" in bin 1. The scatter plots for day 0 and day 1 are well represented as a single population, which means that the cell cycles of *C. zofingiensis* cells are noticeably uniform after preculture. From day 2, each scatterplot shows two populations, corresponding to mature cells (> 60 μm^2) and daughter cells (< 60 μm^2). The former population (> 60 μm^2) has a smaller value of SHG fraction in bin 1 (which indicates that starch exists more uniformly inside of the cells), whilst the latter population (< 60 μm^2) has a larger value of SHG fraction in bin 1 (which indicates that starch is more localized around the center of the cells). Additionally, an anti-correlation between the SHG fraction and the cell size is observed among the mature cells (cell population with a larger cell size). The observed anti-correlation is accounted for by the hypothesis by Fučíková *et al*. [5] that more mature cells have multiple parental chloroplasts while younger cells contain just a single chloroplast. There is another noteworthy finding on the scatter plots, which is that the cell population of daughter cells is shifted to Q4 (higher SHG fraction in bin 1) on day 6 and day 7. This shift indicates that if mature cells were divided into daughter cells on day 5 and day 6, the accumulated starch was more concentrated around the center of the daughter cells, suggesting that the starch in the daughter cells is more centrally localized in the case that they are divided from the parental cells possessing more numerous (4, 8, and 16) nuclei rather than divided from the parental cells with 2 nuclei.

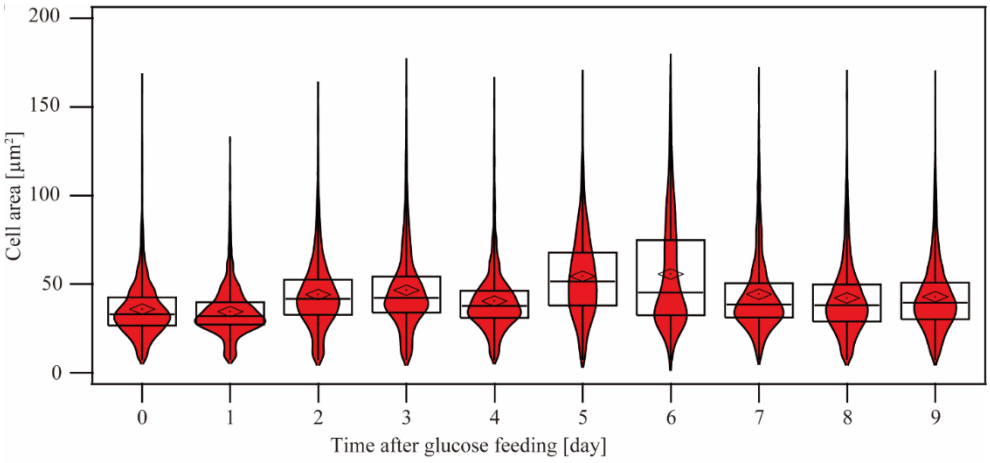

Fig. 3. Changes in *C. zofingiensis* cell size after glucose supplementation.

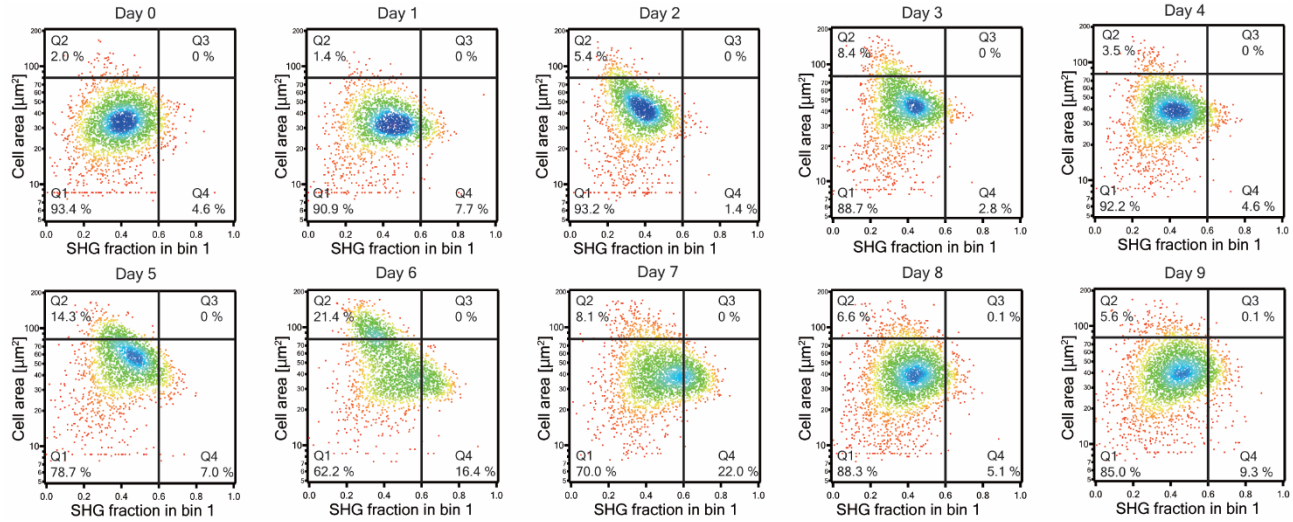

Fig. 4. Scatter plots of SHG fraction v.s. the cell area of *C. zofingiensis* cells from day 0 to day 9 after glucose supplementation.

Conclusion

In this work, I developed a new label-free imaging flow cytometry named label-free multiphoton imaging flow cytometry for high-throughput imaging of noncentrosymmetric materials in living cells and demonstrated its utility by imaging *C. zofingiensis* cells. As a result, it was observed that starch was more evenly present in larger mature cells, which is accounted for by the more mature cells holding a larger number of chloroplasts. Another noteworthy finding was the starch was more centrally localized in the daughter cells on day 6 and day 7, which implies that the starch was more localized if they were newly divided from larger parental cells. The newly developed label-free multiphoton imaging flow cytometry solved the problems of conventional fluorescence-based imaging flow cytometry and paves the way for further statistical microbiological studies, including the metabolic analysis of the interaction of chloroplast-driven photosynthesis and mitochondrial glucose metabolism in microbiological cells.

References

1. Herzenberg, L. A. *et al. Sci. Am.* 234, 108–118 (1976).
2. Lei, C. *et al. Nat. Protoc.* 13, 1603–1631 (2018).
3. Suzuki, Y. *et al. Proc. Natl. Acad. Sci. U. S. A.* 116, 15842–15848 (2019).
4. Kinegawa, R. *et al. Cytom. Part A* 103, 584–592 (2023).
5. Fučíková, K. *et al. Fottea* 12, 83–93 (2012).

Table of contents

1. Introduction

1-1. Flow cytometry

Flow cytometry is a powerful technique to analyze and sort single cells and particles in heterogeneous mixtures at high throughput. By incorporating principles of fluid dynamics, optics, electronics, and data analysis, flow cytometry provides detailed information in a rapid manner. Specifically, not only cell size and shape, but also surface markers on cell membranes, and intercellular molecular properties can be measured and analyzed with a flow cytometer [1–8]. Because of its splendid utility, flow cytometry is widely used in various fields such as immunology, microbiology, molecular biology, and others. For instance, flow cytometry is utilized in immunology as an essential tool for distinguishing and categorizing cell types such as T-cells based on single-cell resolved multi-parametric analysis. In microbiology studies, flow cytometry is employed to classify different types of cells and isolate efficient cells that accumulate valuable molecules such as lipids and carotenoids with a flow cytometer with a cell sorting system. Flow cytometry also plays an important role in microbiology, such as gene expression analysis and intercellular signal pathway analysis by acquiring and analyzing fluorescence signals and evaluations of protein-protein interactions by utilizing fluorescence resonance energy transfer (FRET) in flow cytometry. Moreover, flow cytometry proves its merit in rare-cell detection and isolation owing to its capability of high-speed and successive measurements. Rare cells such as circular tumor cells (CTCs), circular endothelial cells (CECs), minimal residual disease (MRD), and rare subsets of immune cells can be detected and sorted with a flow cytometer, which is challenging with a conventional microscope because of its slow throughput. As shown in the examples above, flow cytometry is nowadays applied to diverse situations. In the subsequent parts of this section, I will trace the history of the development of flow cytometry and then provide an overview of the system's configuration of today's typical flow cytometer.

Flow cytometry began in the late 1940s with the invention of the "Coulter Counter" by Wallace H. Coulter [9]. This Coulter's invention was motivated by the great demand for high-speed and accurate assessments of blood cells in blood. Before the emergence of Coulter Counter, blood cells were counted manually with microscopes, which limited the number of countable blood cells. Coulter provided Coulter Counter as the fundamental solution, which paved the way for today's flow cytometry. A coulter Counter is an electronic device designed to count and measure particles suspended in liquid media. This instrument established the basis for flow cytometry by introducing the concept of impedance-based particle detection, now known as the Coulter principle. The Coulter principle expresses that the electrical impedance changes when particles

suspended in electrically conductive media pass through a small cavity, allowing these particles to be detected and counted. In order to improve the cell counting accuracy, Coulter and his brother devised a refined method to measure the volume of the cell suspension accurately with a mercury manometer and integrated it into the Coulter Counter. As a result of these simple and innovative techniques, the Coulter Counter achieved cell counting at a rate of > 6,000 events/s (about 100 times faster than the conventional manual counting with a microscope) with about 10 times better accuracy than the conventional manual method [10]. Because of its capability of accurate and rapid cell counting, blood cell counting by the Coulter Counter was demonstrated at the National Institute of Allergy and Infectious Disease (NIAID), showcasing its excellent utility in hematology [11]. Moreover, the Coulter's principle also contributed significantly to forming standardized methods for quality testing in a variety of areas, including pharmaceutical, cosmetics, and food industries.

As an expansion of the Coulter Counter, in the advancements in science and technological breakthroughs in the middle of the 20th century, Mack Fulwyler designed and developed an innovative apparatus that enabled not only cell volume measurements but also cell sortings based on the measured cell volumes in 1965 [12]. In the cell sorting system, at the first step, an electric pulse linear to each cell's volume was acquired based on the Coulter principle when the cell passes through an aperture. After this electrical detection stage, the cell was captured into a droplet generated with a piezoelectric element driven at 72 kHz. Following the encapsulating process, the droplet capturing the cell was electrically charged according to the measured cell volume by a charging collar. Then, an electric field between deflection plates separates the electrically charged droplet into the suitable collection containers. With this cell sorting system, he achieved cell separations of human red blood cells, mouse blood cells, and mouse lymphoma cells at a throughput of 500 – 1,000 cells/s, up to 50 percent separation rate, and with a viability of > 96%. This result was incomparably superior in both throughput and accuracy to previous primitive methods, such as manual picking of cells under microscopes, cell separation utilizing centrifuges, and cell filtration with filters with different pore sizes. Moreover, the high viability of Mack Fulwyler's cell sorter also holds significant advantages in its applications, such as cell sorting and cell culturing for regenerative medicine applications. The capability of cell sorting with high viability also means that both time and financial costs can be reduced. Owing to its exceptional utility, Fulwyler's revolutionary electrostatic cell sorting technique has been taken over fluorescence-activated cell sorter as described below and is utilized for high-speed and accurate cell separation in various fields such as life science and microbiology.

As a further advancement of flow cytometry, Leonard Herzenberg *et al.* developed the fluorescence-activated cell sorter (FACS) in the 1970s [13]. FACS integrated the Coulter principle with fluorescence detection and Fulwyler's cell sorting scheme, allowing cell sorting based on the signal from fluorescence markers tagged on the surface of each single cell in flow. FACS was invented to meet the demand to isolate lymphocytes and their mutants in immunological and genomic studies. Isolations of lymphocytes were challenging with utilizing existing methods such as Fulwyler's method based on cellular volume and centrifugation based on cellular density. Hence a new cell sorting method depending on the differences of cell surface structures was required. To address this need, FACS utilized fluorescence markers to tag the cellular surface, subsequently obtaining the cell surface information based on the fluorescence signal. After the fluorescence signal acquisition, each droplet containing a single cell was electrically charged according to the acquired signal intensity in the same manner as Fulwyler's system. The charged droplet was then sorted into appropriate containers by the electric field between deflection plates. As a result, this new type of cell sorting system offered the capability of isolating cells based on set thresholds of fluorescence signal intensity in addition to cellular size with a throughput of 5,000 cells/s and a purity of 90 – 99%, widening its application areas including microbiology and life science.

Fig. 1 shows a schematic of a conventional single-point flow cytometer. As illustrated, a flow cytometer is composed of a hydrodynamic system, excitation light sources, and optical detection systems. The fluidic system is capable of transporting samples with a constant flow speed, ensuring that single cells or particles pass through the device in a single line. This alignment is vital for analyzing individual cells as they pass through the excitation beam without undercounting. An excitation source is also needed to get a signal from the cells, and a variety of lasers are available. Continuous wave (CW) lasers play an essential role in flow cytometry, providing monochromatic coherent light sources for the excitation of fluorophores and the generation of scattering signals. Lasers of various wavelengths can be selected according to the chromophore and the applications. On the other hand, pulse lasers play crucial roles in the excitation for nonlinear optical processes, such as two-photon fluorescence, coherent-anti Stokes Raman scattering, and stimulated-Raman scattering. Multiple lasers can be utilized in a single flow cytometer to excite multiple fluorophores and other biomarkers simultaneously, expanding the range of measurable parameters. A flow cytometer's optical detection system works for selective collections of the scattered and fluorescence signals generated by the interaction between samples and laser light. This detection system commonly comprises some optical elements such as lenses, mirrors, and spectral filters to filter unwanted photons and collect only the optical signal onto

appropriate detectors. The selection and combination of spectral filters are critical for isolating specific wavelengths of light. Spectral filters such as short-pass filters, long-pass filters, and band-pass filters allow the separation of fluorescent signals and other optical signals emitted from samples, increasing the detections' specificities. Photomultiplier tubes (PMT) and avalanche photodiodes (APD) are commonly used for optical signal detections because of their higher quantum efficiencies. The detected optical signals are converted into analog electrical signals by these detectors. Then, the analog signals are digitized and sent to computers by data acquisition (DAQ) systems. Raw data from a flow cytometer is processed on a computer in order to characterize each single cell and properties of selected cell populations and to compare between various experimental conditions. Variable parameters such as mean values, median values, and coefficients of multi-color fluorescence intensities are commonly used for statistical analysis. Moreover, applying advanced statistical methods, including clustering analysis and machine learning algorithms, can also be utilized for revealing patterns and relationships within the data. The analyzed data in flow cytometry can be expressed in various forms, such as histograms, violin plots, scatter plots, and contour plots. The results of these analyses of the acquired data have been applied to variable fields such as microbiology and life science.

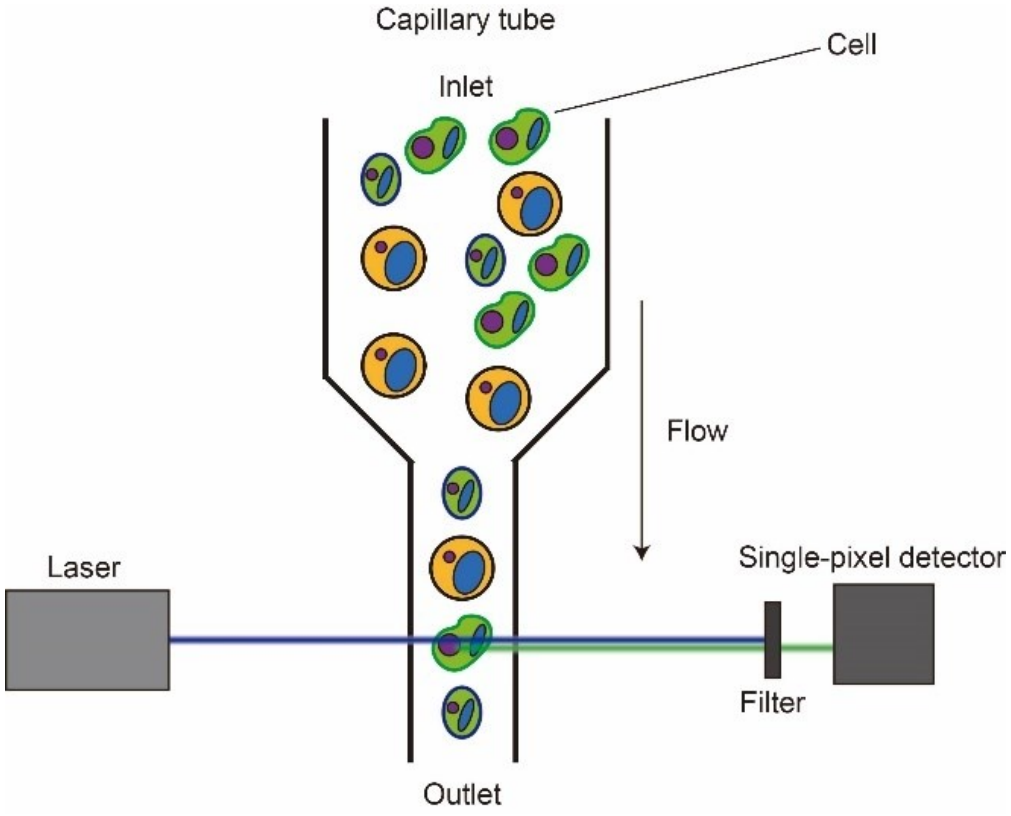

Fig. 1. Schematic of a conventional single-point flow cytometry system.

1-2. Imaging flow cytometry

As described in the previous section, conventional (single-point) flow cytometry is a useful tool for a variety of applications, but it lacks spatial information in return for its high-throughput measurements. Because of this drawback, we cannot obtain morphological information and biomarker distribution within target cells with a single-point flow cytometer.

On the other hand, imaging flow cytometry is capable of high-throughput single-cell "imaging" by incorporating the schemes of flow cytometry and fluorescence microscopy (Fig. 2). So far, various schemes for acquiring continuous single-cell images in flow have been demonstrated. In the case of adopting methods to illuminate a whole single cell at the same time, such as wide-field excitation [14] and light-sheet excitation [15–19], a cellular image can be obtained by utilizing a multi-pixel detector such as a charge-coupled device (CCD) camera with time-delay integrations (Generally < 100 MHz) [14,20] and a faster complementary metal oxide semiconductor (CMOS) camera [15–18]. Recently, techniques such as virtual-freezing fluorescence imaging (VIFFI) [17,18] have been demonstrated to improve signal-to-noise ratio (SNR) without dropping its throughput by gaining longer exposure time to flowing cells in a microfluidic channel. In the case of employing an illumination scheme of scanning a beam spot on a cell using optical scanners [21] or acousto-optic deflectors (AODs) [21–24] , conversely, the fluorescence signal from each point on the cell can be detected by a single-pixel detector with high sensitivity and fast sampling rate (> 1 GS/s), such as avalanche photodetector (APD) or a photomultiplier tube (PMT). Following the signal detection, a fluorescence image can be constructed based on the acquired signals on a computer. By reducing the volume of illumination, the photon flux on the sample can be increased, leading to the improvement of two-photon fluorescence intensity due to its nonlinearity. Besides, high-speed fluorescence imaging flow cytometry at a rate of up to 16,000 frames/s [21] has been demonstrated with the combination of a rapid beam scanning scheme and a high-speed single-pixel detector. Owing to its efficacy, imaging flow cytometry has been employed across a wide range of fields in research in biology and life science, as described in this section.

Owing to its efficacy, imaging flow cytometry has been employed across a wide range of fields in research in biology and life science, as follows. One of the application targets of imaging flow cytometry is cell-cell interaction analysis. For example, the interaction between circular tumor cells (CTCs) and dendritic cells (DCs) was visualized and analyzed by imaging flow cytometry [25]. Before this work was demonstrated, conventional single-point flow cytometers were used for this purpose with limitations. In the CTCs and DCs interaction measurements with a conventional single-point flow cytometer, CTCs and DCs are labeled with

different color tags, and the dual color fluorescence signals from them are recorded as pulses with two different channels. When CTCs and DCs interact with each other, these pulse signals overlap in the temporal domain. So, analysis of the overlap between the two-color signals works as an indicator of these cells' interaction. Nonetheless, this single point detection method cannot provide spatial information of cells, missing important morphological information such as if cells are single cells or CTC clusters, and the size of the clusters. This limitation was solved with imaging flow cytometry due to its imaging capability. In imaging flow cytometry, single cells and clusters could be easily distinguished by the taken images of labeled cells. Further analysis revealed that the flowing velocity of the CTC-DC cluster is slower than the single DC and the DC cluster. The slow migration of CTC-DC clusters may bring a new finding into the metastasis of cancer.

One of the other interesting phenomena that can be measured by imaging flow cytometry is phagocytosis [26]. Phagocytosis is a vital immune system process in which antigen particles are taken up by some type of cells, such as macrophages and neutrophils [27]. Because of its capability of image capturing, imaging flow cytometry provides image data with information on the number of particles taken up by phagocytosis and their localizations within cells. Based on the image data analysis, the effect of the environmental temperature on the efficiency of phagocytosis can be evaluated statistically [28], which could not be achieved by conventional single-point flow cytometry.

Extracellular vesicles (EVs) analysis was also demonstrated by imaging flow cytometry [20,29]. Various types of nano- and micron-sized membrane-coated particles are released from cells into the extracellular environment. These EVs are classified into different subtypes, such as exosomes (70-150 nm) and microvesicles (100-1000 nm). They are assembled in cell-type-dependent ways to act as mediators for complex intercellular interactions, both locally (autocrine signaling and paracrine signaling) and remotely (endocrine signaling), under both pathological and healthy states [30]. So, they are gaining increasing recognition as potential biomarkers and remedial agents [30,31]. Conventional flow cytometers typically cannot detect objects smaller than 200-300 nm and are essentially blind for small EVs (sEV) [32]. On the contrary, imaging flow cytometers are able to detect sEVs tagged with enhanced Green Fluorescent Protein (eGFP) and even distinguish single sEVs in complex samples with cells without any prior preparation [20]. The capability of imaging flow cytometry would be helpful for a better understanding of EV's heterogeneity from functional perspectives. In addition to the above, imaging flow cytometry is also used in a variety of research areas, such as subcellular localization of signaling molecules [15,33] and cell-cycle analysis [34,35].

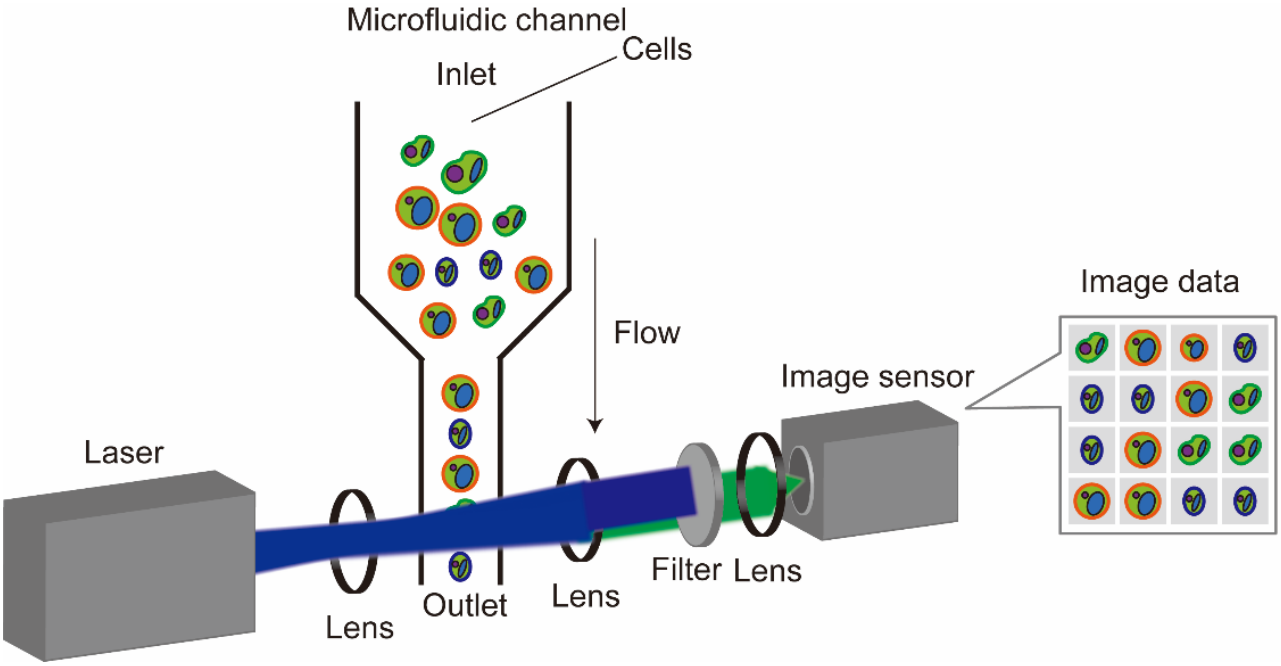

Fig. 2. Schematic of imaging flow cytometer.

1-3. Label-free imaging flow cytometry

In spite of its great capabilities of identification and classification of individual single cells based on captured fluorescence images as described in the last section, fluorescence imaging flow cytometry remains drawbacks due to its labeling such as required both time and financial costs, cytotoxicity, its non-specific bindings and potential interferences with small molecules' functions, and challenges in labeling intracellular molecules [36]. Label-free imaging flow cytometry is emerging as a valuable tool for research in biology and life science, overcoming technical constraints in traditional fluorescence-based imaging flow cytometry mentioned above. Until now, mainly two different types of label-free imaging flow cytometry have been demonstrated in addition to conventional bright-field imaging flow cytometry.

First, optofluidic time-stretch flow cytometry was developed for quantitative phase imaging [37,38]. It captures quantitative phase images of large numbers of single cells at high event rates of over 10,000 events per second (eps) [37]. Optofluidic time-stretch quantitative phase imaging flow cytometry enabled large-scale analysis and screening of large amounts of single cells using computational approaches such as compressive sensing and machine learning. This method has so far been demonstrated, with the aid of machine learning, for high-speed imaging of leukocytes for drug screening [39,40], detection and classification of aggregating platelets [41,42] and screening for leukemia [43].

Next, vibrational imaging flow cytometry via stimulated Raman scattering (SRS) was developed [44]. SRS imaging flow cytometry provided chemical images of intracellular molecules based on their Raman signal intensities with a throughput of up to 140 eps. This technique enabled visualization of intracellular contrast of lipid, paramylon, and chlorophyll in *E. gracillis* cells, letting a classification of the cells cultured under different conditions with an accuracy of > 99%. Marker-free cancer cell detection was also demonstrated with SRS imaging flow cytometry based on SRS contrast images of protein, lipids, and hemoglobin SRS imaging flow cytometry.

Even with the progress of optofluidic time-stretch imaging flow cytometry and SRS imaging flow cytometry, the entire characterization of a broad range of complex biological systems in a label-free way still remains challenging because of the limited information acquired by these methods. Especially optofluidic quantitative time-stretch phase imaging lacks the ability to provide chemical specificity, thus failing to assess the chemical composition of cells while providing three-dimensional morphological details of single cells. Conversely, SRS imaging flow cytometry provides chemical specificity, but its chemical imaging capabilities are limited by small Raman scattering cross-sections of biomolecules (10-30 cm^2/sr) [45] and the narrow bandwidth of SRS (typically limited to a high wavenumber range from 2,800 to 3,200 cm^{-1}), which stems from the scarcity of available laser sources. Besides those two methods, though other types of label-free imaging flow cytometry, such as bright-field imaging flow cytometry [34,46,47] and dark-field imaging cytometry [47,48] are reported, they also hold the same drawback of lacking chemical specificity as optofluidic time-stretch flow cytometry. Even though the fusion of label-free imaging and machine learning has certainly advanced the biological understanding extracted from the collected images, accessing more chemical details at the raw data level is vital for leveraging the full potential of label-free imaging flow cytometry. Especially, it is still challenging to carry out imaging of some key biomolecules, such as starch and collagen, by label-free imaging flow cytometry.

1-4. Goal of this thesis

As described in the last section, it had still been difficult to perform imaging of starch and collagen with the existing label-free imaging flow cytometer. The goal of this thesis was to observe these molecules within cells and track the changes in their amounts and intracellular distributions in a statistical manner to deepen the knowledge in microbiology and life science, which was challenging to achieve by using existing label-free imaging flow cytometers or other methods such as bright-field microscopes and slow throughput electron

microscopes. To achieve this goal, the development of a new type of label-free imaging flow cytometer that broadens the range of accessible intracellular information was essential.

In this thesis, I developed a new variety of label-free imaging flow cytometry for high-throughput visualization of starch and collagen in living cells: label-free multiphoton imaging flow cytometry [49]. My multiphoton imaging flow cytometer provides nonlinear optical images, where image contrast is produced by two kinds of nonlinear optical effects: second-harmonic generation (SHG) and four-wave mixing (FWM). SHG is an optical effect resulting from the second-order optical susceptibility of materials and is employed to visualize starch [50], collagen [51], and other non-centrosymmetric materials [52]. On the other hand, four-wave mixing (FWM) is a third-order nonlinear optical process that occurs under the presence of intense light and involves the interaction of three initial light waves with samples, resulting in the generation of a fourth wavelength. Notably, FWM has been utilized for high-contrast label-free visualization of cytoplasm within cells [53–55]. The multiphoton imaging flow cytometer consists of a microfluidic system, a dual color (SHG and FWM) microscope with a 2D-scanned focused beam, and a fast signal acquisition circuit designed to simultaneously capture SHG and FWM images of flowing cells. The reason why I adopted the raster-scan configuration rather than a wide-field or light-sheet illumination scheme for the multi-photon imaging flow cytometer is that the efficiencies of SHG and FWM are remarkably increased under stronger light fields by virtue of their nonlinear processes. Consequently, the multi-photon imaging flow cytometer can acquire SHG and FWM images with a pixel resolution of 100 × 100 pixels, a spatial resolution of 500 nm, a field of view of 50 μm × 50 μm, and an intensity depth of 14-bit at a high event rate of 4-5 event per second, equivalent to a throughput of 560-700 kb/s.

In order to demonstrate the potential of my multiphoton imaging flow cytometer, I applied the system to analyze *Chromochloris zofingiensis* (NIES-2175), a type of green algae, which have recently attracted industrial attention due to its capability to efficiently produce valuable materials for bioplastic [56,57], biofuel [58], and food [59]. There is currently a strong need to optimize the culture conditions of *C. zofingiensis* cells for enhancing their starch production efficiency. Traditionally, starch accumulated in *C. zofingiensis* cells is measured by Lugol staining [60] or colorimetric analysis [61]. However, these methods necessitate cell fixation, expensive consumables, and lengthy protocols. In addition, colorimetric assays collectively measure the amount of accumulated starch in bulk in terms of weight per biomass unit, thus losing crucial information on cellular heterogeneity that is indispensable for understanding cellular metabolism with a single-cell resolution. My multiphoton flow cytometer solved this challenge by characterizing cell size, intracellular starch content,

and its spatial distribution without any labeling. As a practical demonstration, I captured 2,000 SHG and FWM images of *C. zofingiensis* cells using the multiphoton flow cytometer 0-9 days after refreshing the culture medium. Analysis of the acquired images revealed that synthesized starch was centrally located in the cell during the early stages of the cell cycle and delocalized during the late stages. Label-free multiphoton imaging flow cytometry paves the way for richly detailed statistical studies of biological functions and optimization of the development of highly productive cell lines.

2. Methods

2-1. Theory

As described in section 1-4, my label-free imaging flow cytometry adapts two kinds of nonlinear optical processes: second-harmonic generation (SHG) and four-wave mixing (FWM). SHG is utilized for the visualization of intracellular noncentrosymmetric materials, while FWM is employed for acquiring cellular outlines. In this section, I will explain the background theories of SHG and FWM, respectively.

2-1-1. Second-harmonic generation (SHG)

SHG is a second-order nonlinear optical process resulting from interactions between noncentrosymmetric materials and intense light fields. The induced second-order polarization for the material is expressed as [62–64]

$$\boldsymbol{P} = \boldsymbol{\chi}^{(2)}\boldsymbol{E}\boldsymbol{E} \tag{1}$$

where $\boldsymbol{P}$ is the second-order polarization caused by the interaction between light and a material, $\boldsymbol{\chi}^{(2)}$ is a second-order optical susceptibility of the material, and $\boldsymbol{E}$ is the electric field vector of the incident light, respectively.

In the case that the material has a center symmetricity, substituting $-\boldsymbol{E}$ into $\boldsymbol{E}$ in the right side of the equation (1) yields $-\boldsymbol{P}$ as follows.

$$\begin{aligned} -\boldsymbol{P} &= \boldsymbol{\chi}^{(2)}(-\boldsymbol{E})(-\boldsymbol{E}) \\ &= \boldsymbol{\chi}^{(2)}\boldsymbol{E}\boldsymbol{E} \end{aligned} \tag{2}$$

By comparing the equation (1) and (2), the induced second-order polarization $\boldsymbol{P} = 0$ if the material is centrosymmetric. Because of this nature, SHG is used for imaging of noncentrosymmetric materials, such as endogenic starch [50], collagen [51], and myosin [65], as well as exogenic SHG tags [52].

Jablonski energy diagram of SHG can be described as Fig. 3. In the process of SHG, strong light fields interact with samples and induces second-order optical polarization as described in the equation (1), generating a new photon with double energy (double frequency) (Fig. 4). The relationship between the SHG signal intensity and the properties of the incident pulse can be considered as below. The incident pulse is well approximated as a Gaussian.

$$\boldsymbol{I}(\boldsymbol{t}) = \mathbf{A}\exp\left(-\mathbf{b}\boldsymbol{t}^{\boldsymbol{2}}\right) \tag{3}$$

where $\boldsymbol{I}(\boldsymbol{t})$ is the pulse intensity in time domain, **A** and **b** are coefficients for amplitude and pulse duration, respectively. Under this assumption, the pulse energy $\boldsymbol{Q}$ and the full width at half maximum (FWHM) of the pulse duration $\boldsymbol{\tau}_{\mathbf{pulse}}$ are expressed as follows.

$$Q = A\sqrt{\frac{\pi}{b}} \tag{4}$$

$$\tau_{pulse} = 2\sqrt{\frac{\ln(2)}{b}} \tag{5}$$

From the equation (1), (4), and (5), the relationship between SHG signal intensity, the incident pulse energy and pulse duration are derived as follows.

$$I_{SHG} \propto |P|^2$$

$$\propto \int \chi^{(2)^2} I(t)^2 \, dt$$

$$= |\chi^{(2)}|^2 \int A^2 \exp(-2bt^2) \, dt$$

$$= |\chi^{(2)}|^2 A^2 \sqrt{\frac{\pi}{2b}}$$

$$\propto \frac{Q^2}{\tau_{pulse}} \tag{6}$$

As shown in the equation (6), SHG signal intensity is enhanced quadratically by increasing incident laser power as well as by shortening pulse duration.

Next, a schematic of spectral profile of SHG signal and a fundamental beam is depicted as Fig. 4. An intensity profile of an input pulse in spectral domain can be approximated as Gaussian

$$I_{pulse}(\lambda) = \alpha \exp\left[-\beta(\lambda - \lambda_{center})^2\right] \tag{7}$$

where α and β are coefficients for amplitude and spectral width, and λ_{center} is a center wavelength of the input pulse, respectively. Under this approximation, FWHM of the spectral width of the input pulse is expressed as follows.

$$\sigma_{pulse} = 2\sqrt{\frac{\ln(2)}{\beta}} \tag{8}$$

From the equation (7), the spectral profile of the SHG signal is derived as follows. (Note that the wavelength of the SHG signal is half that of the fundamental beam.)

$$I_{SHG}(\lambda) \propto \left|I_{pulse}(2\lambda)\right|^2$$

$$= \left\{\alpha \exp\left[-\beta(2\lambda - \lambda_{center})^2\right]\right\}^2$$

$$= \left\{\alpha \exp\left[-4\beta\left(\lambda - \frac{\lambda_{center}}{2}\right)^2\right]\right\}^2$$

$$= \alpha^2 \exp\left[-8\beta\left(\lambda - \frac{\lambda_{center}}{2}\right)^2\right] \quad (9)$$

With the equation (9), the FWHM of SHG signal can be calculated as below.

$$\sigma_{SHG} = 2\sqrt{\frac{\ln(2)}{8\beta}} = \sqrt{\frac{\ln(2)}{2\beta}} \quad (10)$$

From the equation (8) and (10), the ratio between the FWHM of SHG spectral width and spectral width of the fundamental beam is

$$\gamma \equiv \frac{\sigma_{SHG}}{\sigma_{pulse}} = \frac{1}{2\sqrt{2}} \quad (11)$$

Though some previous articles reported that the ratio between the FWHM of the spectral width of SHG and an input pulse is $\frac{1}{\sqrt{2}}$ [63,66], it is incorrect. Tobias *et al.* proved that the factor is $\frac{1}{2\sqrt{2}}$, both theoretically and experimentally [67]. This value is helpful information for selecting bandpass filters with suitable bandwidth for SHG detection. Moreover, the SHG's spectral information is critically important to confirm that there is no spectral overlap with other light, such as the fundamental beam and fluorescence, which is necessary for multi-color imaging.

The square of the illumination point spread function (IPSF) is a factor that limits the spatial resolution in imaging with two-photon excitation, and the square of the IPSF is approximated as follows [68].

$$\omega_{XY} = \frac{0.320\lambda}{\sqrt{2}NA} \quad (12)$$

$$\omega_Z = \frac{0.532\lambda}{\sqrt{2}}\left(\frac{1}{n - \sqrt{n^2 - NA^2}}\right) \quad (13)$$

where ω_{XY} and ω_Z represents the lateral and axial width at the 1/e of the maximum of the intensity squared value, respectively. λ is the wavelength of the fundamental laser. NA is the numerical aperture of the objective lens, and n is the refractive index of the medium. In the case of the developed label-free multiphoton imaging flow cytometer, ω_{XY} and ω_Z are calculated as $\omega_{XY} = 280$ (nm) and $\omega_Z = 1.3$ (μm) by the substitution of λ = 800 (nm), NA = 0.65, and n = 1.0. Note that the lateral spatial resolution of the developed label-free imaging flow cytometer is limited by the pixel size of 500 nm.

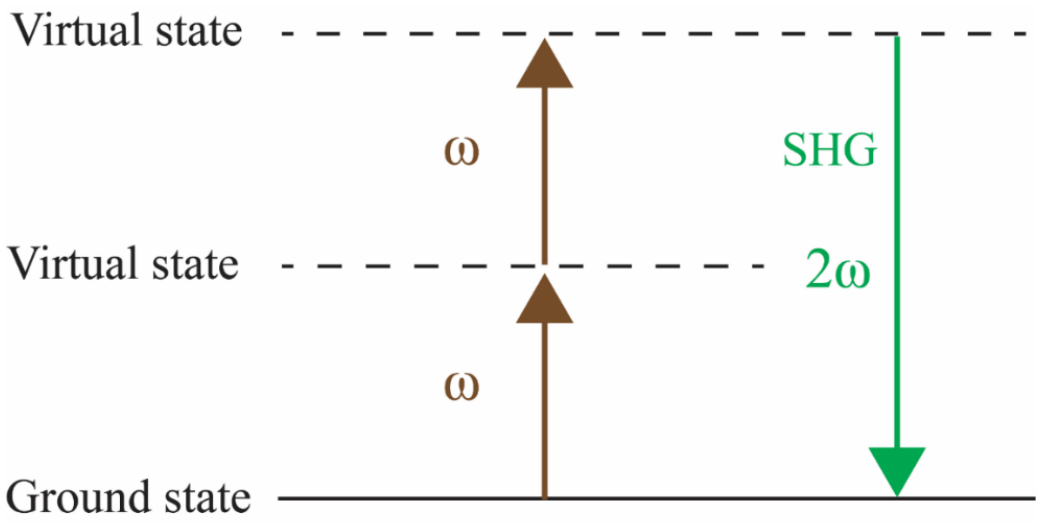

Fig. 3. Jablonski energy diagram of SHG. In the process of SHG, two photons are converted into a new photon with a double frequency.

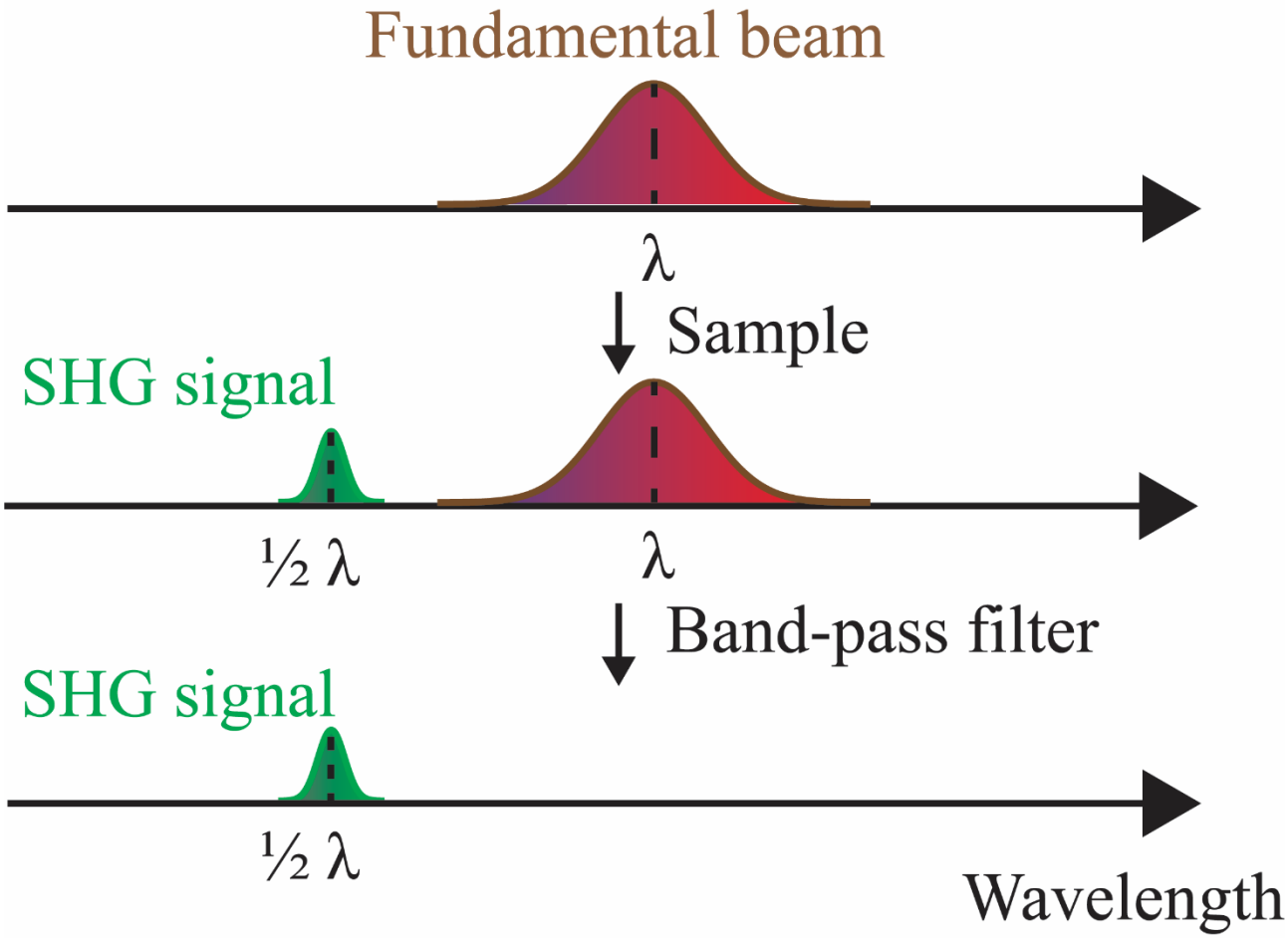

Fig. 4. Schematic of the spectral shift of SHG signal from a fundamental beam. The center wavelength of SHG is half of that of the fundamental beam.

2-1-2. Four-wave mixing (FWM)

FWM is a third-order nonlinear optical process where three input waves interact with a sample and generate a new fourth wave [54]. FWM imaging allows us to visualize the contrast based on the distribution of third-order nonlinear optical susceptibility of intracellular molecules [53–55] as well as nanoparticles [54,69].

In FWM processes, the induced polarization can be expressed as [53,55]

$$\boldsymbol{P}(-\boldsymbol{\omega_4}) = \boldsymbol{\chi}^{(3)}(-\boldsymbol{\omega_4};\boldsymbol{\omega_1},\boldsymbol{\omega_2},-\boldsymbol{\omega_3})\boldsymbol{E}(\boldsymbol{\omega_1})\boldsymbol{E}(\boldsymbol{\omega_2})\boldsymbol{E}(-\boldsymbol{\omega_3}) \quad (14)$$

where $\boldsymbol{P}(-\boldsymbol{\omega_4})$ is the induced polarization caused by the interaction between incident light and matters, $\boldsymbol{\chi}^{(3)}(-\boldsymbol{\omega_4};\boldsymbol{\omega_1},\boldsymbol{\omega_2},-\boldsymbol{\omega_3})$ is the third-order optical susceptibility, $\boldsymbol{E}$ is the electric field vector of the incident light, respectively. In the equation (14) the positive signs of frequencies ($\boldsymbol{\omega_1}$ and $\boldsymbol{\omega_2}$) mean the frequencies of destroyed photons, whereas the negative signs of frequencies ($-\boldsymbol{\omega_3}$ and $-\boldsymbol{\omega_4}$) are the generated photons' frequencies. Moreover,

$$\boldsymbol{\omega_4} = \boldsymbol{\omega_1} + \boldsymbol{\omega_2} - \boldsymbol{\omega_3} \quad (15)$$

is satisfied as illustrated Jablonski energy diagram in Fig. 5 [53]. In FWM with a single pulse laser source, the frequency of the FWM signal is both blue-shifted and red-shifted from the fundamental beam (Fig. 6). By putting a long-pass filter and a shot-pass filter before and after the sample, blue-shifted FWM signal, which is spectrally separated from autofluorescence from the sample, can be selectively collected [49,55].

Next, the relationship between FWM signal intensity and the the properties of incident pulse can be derived from the equations (3), (4), (5), and (15) as follows.

$$\begin{aligned}
\boldsymbol{I_{FWM}} &\propto |\boldsymbol{P}(-\boldsymbol{\omega_4})|^2 \\
&\propto |\boldsymbol{E}(\boldsymbol{\omega_1})\boldsymbol{E}(\boldsymbol{\omega_2})\boldsymbol{E}(-\boldsymbol{\omega_3})|^2 \\
&\propto \int \boldsymbol{I}(\boldsymbol{t})^3 \, \boldsymbol{dt} \\
&= \int \mathbf{A}^3 \exp(-3\mathbf{b}\boldsymbol{t}^2) \, \boldsymbol{dt} \\
&= \mathbf{A}^3\sqrt{\frac{\boldsymbol{\pi}}{3\mathbf{b}}} \\
&\propto \frac{\boldsymbol{Q}^3}{\boldsymbol{\tau_{pulse}}^2}
\end{aligned} \quad (16)$$

where $\boldsymbol{I_{FWM}}$ is FWM signal intensity, $\boldsymbol{Q}$ is the incident pulse energy, and $\boldsymbol{\tau_{pulse}}$ is the FWHM of input pulse duration, respectively. As derived in the equation (16), FWM signal intensity is proportional to the cube of input pulse energy, while FWM signal intensity is proportional to the inverse of the square of the input pulse

duration. As shown in the equation (6) and (16), both SHG and FWM signal intensity can be enhanced by shortening the input pulse duration without the need to increase laser power. FWM is more sensitive to the input pulse duration, therefore pulse compression can be done easier by first making a rough adjustment based on SHG signal intensity and then fine-tuning based on FWM signal intensity [70].

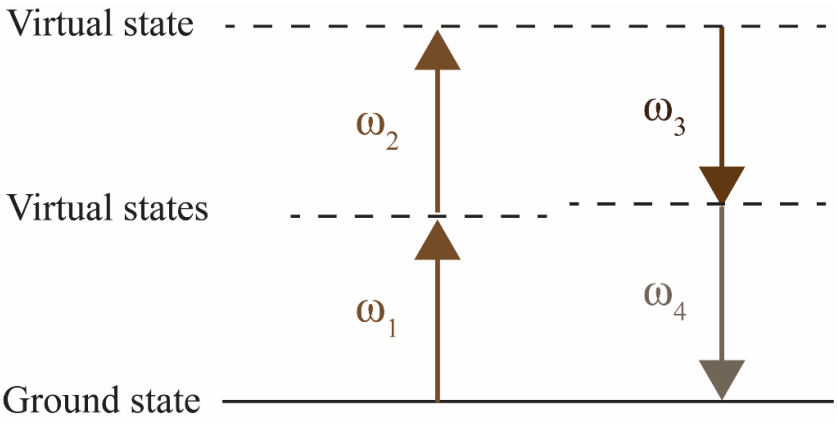

Fig. 5. Jablonski energy diagram of FWM. Input laser pulses interact with materials and fourth wave with the frequency of $\boldsymbol{\omega_4 = \omega_1 + \omega_2 - \omega_3}$ is generated.

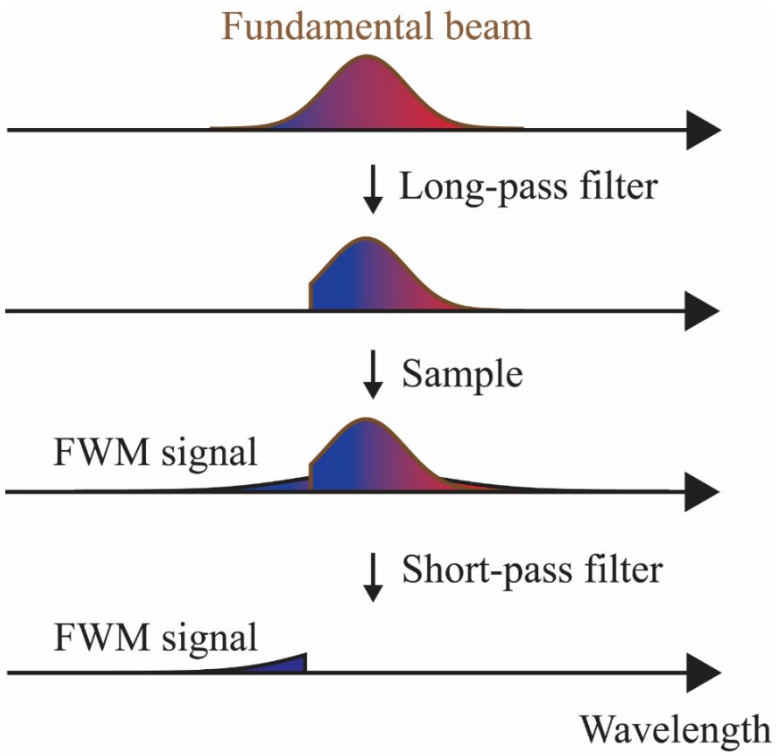

Fig. 6. Spectral shift of FWM signal from the fundamental beam. A combination of a long-pass filter and a short-pass filter enables us to separate the FWM signal from the fundamental beam.

2-2-1. Schematic of label-free multiphoton imaging flow cytometer

The schematic of my label-free multiphoton imaging flow cytometer is depicted as Fig. 7. In the flow cytometer, in the beginning, cultured cells are transferred from Petri dishes to syringes. Then, these cells in syringes are delivered into a microfluidic chip (SC-BU-300300-L, Translume) by a syringe pump (Pump 11 Elite, Harvard Apparatus). The flow speed of cells is controlled as 2 mm/s by the pump. Flowing cells in the microfluidic chip are centrally focused into a single line by acoustic focusing with a piezoelectric element (2.44Z25*30R-SYX(C-213), Nihon Denkei Co., Ltd.), which is attached on the rear side of the microfluidic chip. At the moment that each cell goes through a focused beam spot of HeNe laser (HNL020LB, Thorlabs), a change in the direction of the forward-scattered beam is registered by a Si avalanche photodetector (APD120A/M, Thorlabs), triggering multiphoton imaging (SHG and FWM imaging). Flowing cells then arrive at the SHG and FWM imaging section. A Ti:sapphire laser (Synergy, Spectra Physics) with a FWHM of temporal pulse duration of 17 fs, a repetition rate of 75 MHz, a central wavelength of 793 nm, and a FWHM of spectral bandwidth of 43 nm. A 2D-galvanometric scanner (6210H, Cambridge Technology) is controlled by a triangle wave at 5 Hz (slow axis) and another triangle wave at 500 Hz (fast axis) so that the incident laser beam is scanned over 150 μm in 100 ms (along the stream direction) and 50 μm at 5 Hz (perpendicular to the stream direction) on the focal plane. For the separation of the SHG signal from others, three band-pass filters (FBH400-40, Thorlabs) with a center wavelength of 400 nm and a FWHM of bandwidth of 40 nm. Then, the SHG signal is detected by a photomultiplier tube (H7732-01, Hamamatsu Photonics) with a quantum efficiency of about 20% around 400 nm. A wideband amplifier unit (C6438-01, Hamamatsu Photonics) connected to the photomultiplier tube (PMT) amplified the output signal from the PMT by a factor of 25 mV/μA. On the other hand, respectively positioned a long-pass filter (FELH0750, Thorlabs) with a cut-on frequency of 750 nm and a short-pass filter (FESH0750, Thorlabs) with a cut-off frequency of 750 nm before and after the microfluidic chip for collecting a blue-shifted FWM signal from cells selectively. The FWM signal is detected by an avalanche photodetector (APD120A/M, Thorlabs), whose peak of the sensitivity curve is around 700 - 900 nm. The SHG and FWM signals are converted to digital signals by a 14-bit digitizer (ATS9440, AlazarTech) set its sampling rate of 1 MS/s. A transistor-transistor logic output signal which is synchronized with one frame of imaging (i.e., a single trip of the scanner at 5 Hz) is sent to the digitizer. Output signals from a position sensor integrated into the galvanometric scanner at 500 Hz are also transferred to the DAQ board. These signals are processed on *Igor* (See section 2-3 for details) to construct SHG and FWM images. Accordingly, the label-free

multi-photon imaging flow cytometer allows SHG and FWM imaging with a size of 50 x 50 μm, a pixel density of 100 x 100 pixels, and at a throughput of 10 images/s.

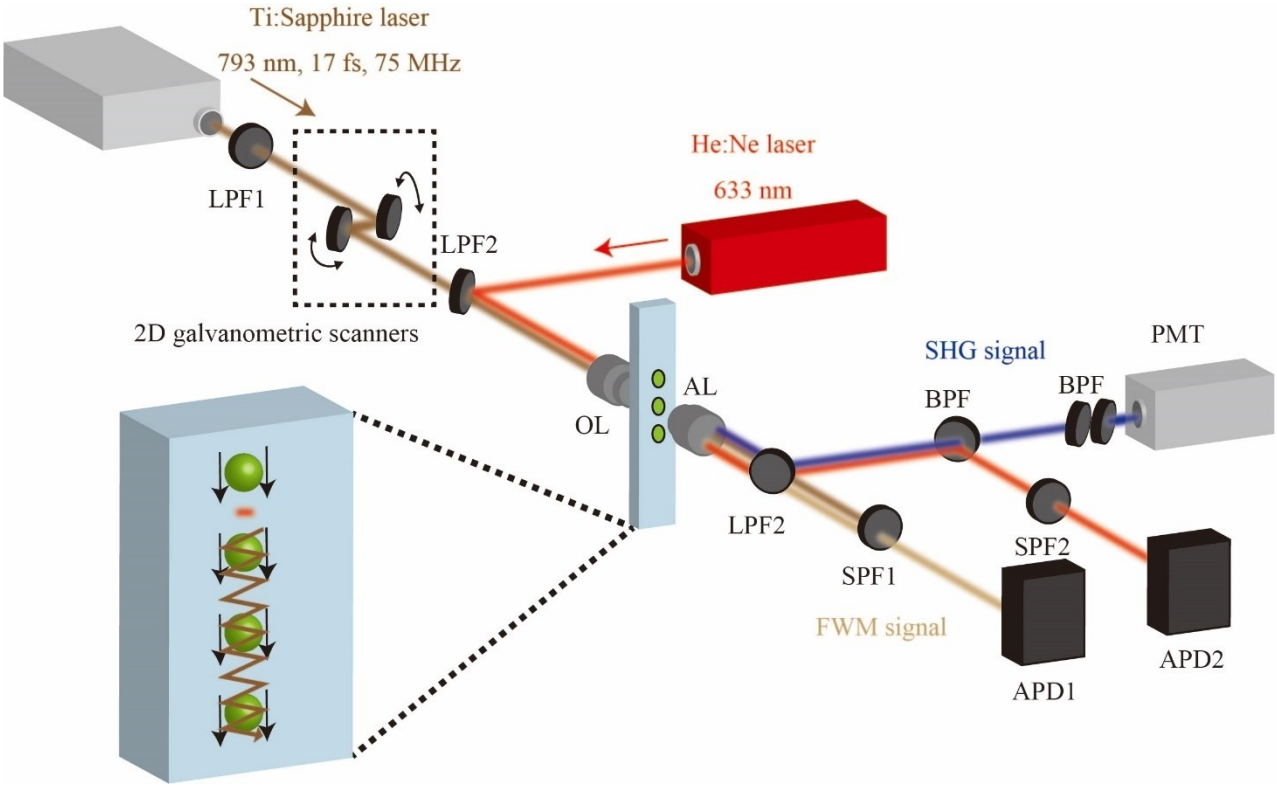

Fig. 7. Schematic of label-free imaging flow cytometer. Cells in syringes are delivered into a microfluidic chip by a syringe pump and then focused into a single line by acoustic force from a piezoelectric element. At the moment that each cell goes through a focused beam spot of the HeNe laser, a change in the direction of the forward-scattered beam is registered by a Si avalanche photodetector, triggering multiphoton imaging. Flowing cells then arrive at the SHG and FWM imaging section. A 2D-galvanometric scanner scans Ti:sapphire laser beam on the focal plane. Three band-pass filters with a center wavelength of 400 nm and a bandwidth of 40 nm are used for selective detection of SHG signal with a photomultiplier tube. A long-pass filter with a cut-on frequency of 750 nm and a short-pass filter with a cut-off frequency of 750 nm are positioned before and after the microfluidic chip for collecting a blue-shifted FWM signal selectively.

2-2-2 Microfluidic system

I utilized a retail available microfluidic chip made of fused silica (SC-BU-300300-L, Translume) for the label-free multiphoton imaging flow cytometer without any requirement of lithography by myself. I glued a market-ready piezoelectric element (2.44Z25*30R-SYX(C-213), Nihon Denkei Co., Ltd.) on the rear side of the microfluidic chip as shown in Fig. 8. The piezoelectric element is connected to an RF signal generator (DSG815, Rigor) with an amplifier (HSA4101, NF corporation) when the flow cytometer is in use. To focus flowing cells into a single line at the center of the channel of the microfluidic chip, the signal generator with the amplifier applies voltage with an amplitude of 7 V at a frequency of 2.62 MHz on the piezoelectric element to produce standing acoustic waves for acoustic focusing. As a note, a piezoelectric element converts received voltage signals into mechanical vibrations, which vibrate the microfluidic chip's wall. The wall's vibrations at the resonant frequency generate acoustic standing waves. In the case that the wavelength of the standing wave is twice the width of the microfluidic channel (regarding the case of this experiment, when voltage signals at 2.62 MHz are applied to the piezoelectric element), a pressure node is created at the center of the channel, allowing acoustic focusing of cells into a single line [71].

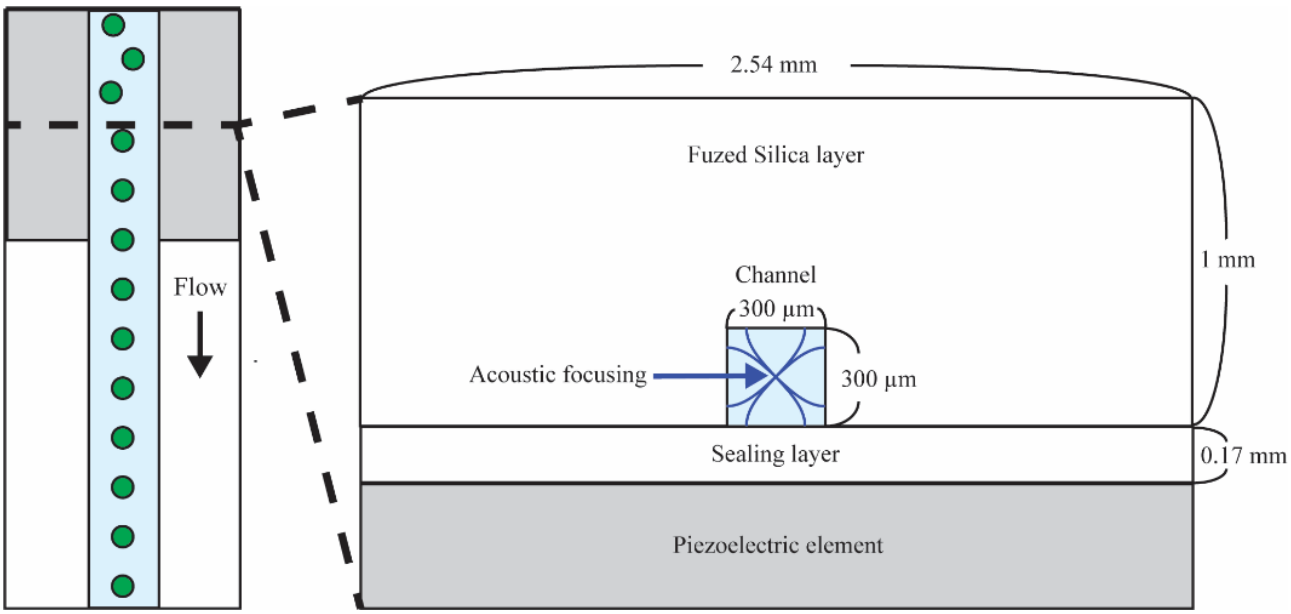

Fig. 8. A schematic of a microfluidic chip used in the label-free multiphoton imaging flow cytometer.

2-3. Working principle of label-free multiphoton imaging flow cytometry

In this section, I describe how the acquired signals from the label-free multiphoton imaging flow cytometer are processed to construct FWM and SHG images and then extract cellular information, such as cell size, volume of intracellular noncentrosymmetric material, and spatial distribution of noncentrosymmetric material inside of cells. As presented in Fig. 9, the TTL voltage signal, the output signal at 500 Hz from the position sensor of the fast axis of the 2D-galvanometric scanner, the FWM signal detected with a Si avalanche photodetector, and the SHG signal amplified and detected by a PMT with an amplifier are sent to the channel 1, 2, 3, 4 of the DAQ board, respectively. The DAQ board samples with a 14-bit intensity resolution at a sampling rate of 1 MS/s and converted these analog signals to digital signals. The raw data is loaded on *Igor 8.04* and processed with a code [Appendix.1] to construct SHG and FWM images with 100 x 100 pixels resolution and saved as tiff files. Examples of constructed FWM and SHG images of *Chromochloris zofingiensis* (NIES-2175) are shown in Fig. 10. The rescaled images are also put on the figure to enhance the visibility of the cells and contents of them. This intensity rescaling process was performed on *ImageJ 1.53e*.

As a next step, the tiff files of FWM and SHG images were analyzed on *Cellprofiler 4.1.3* as shown in Fig. 11. Fig. 11 (a) is an original constructed FWM image. In order to get rid of the background from the original image, 10 pixels are cropped from the top edge of the image using the “Crop” function (Fig. 11 (b)). Then, this cropped part was resized to be the same pixel size as the original image through the “Resize” module with the “Bicubic interpolation method” (Fig. 11 (c)). Subtraction of background (Fig. 11 (c)) from the original FWM image (Fig. 11 (c)) produced a background-free FWM image (Fig. 11 (d)). Following this, I obtained a binary image (Fig. 11 (e)) from the background-free FWM image (Fig. 11 (d)) by the “Threshold” module with the “thresholding method of Otsu”. Thereafter, the cellular outline (Fig. 11 (f)) was extracted from the binary image (Fig. 11 (e)) via the "IdentifyPrimaryObject” module. Based on the cellular outline, each single cell’s size was measured and output. In the same way as the FWM image processing above (Fig. 11 (a-f)), the original SHG image (Fig. 11 (g)) was loaded on *Cellprofiler 4.1.3,* trimmed as shown in Fig. 11 (h), and resized (Fig. 11 (i)). Then, the background subtracted SHG image (Fig. 11 (j)) was obtained by the subtraction of Fig. 11 (i) from Fig. 11 (g). Fig. 11 (k) and (l) are a FWM image overlayed with a cellular outline (green) and an SHG image overlayed with a cellular outline (green), correspondingly. With the “MeasureObjectiveSizeShape” module, I obtained each cell’s area. In addition, the total SHG intensity value on pixels within the cellular outline was acquired using the “MeasureObjectIntensity” module. Furthermore, the intracellular spatial

distribution of SHG intensity value was calculated by means of the “MeasureObjectIntensityDistribution” module.

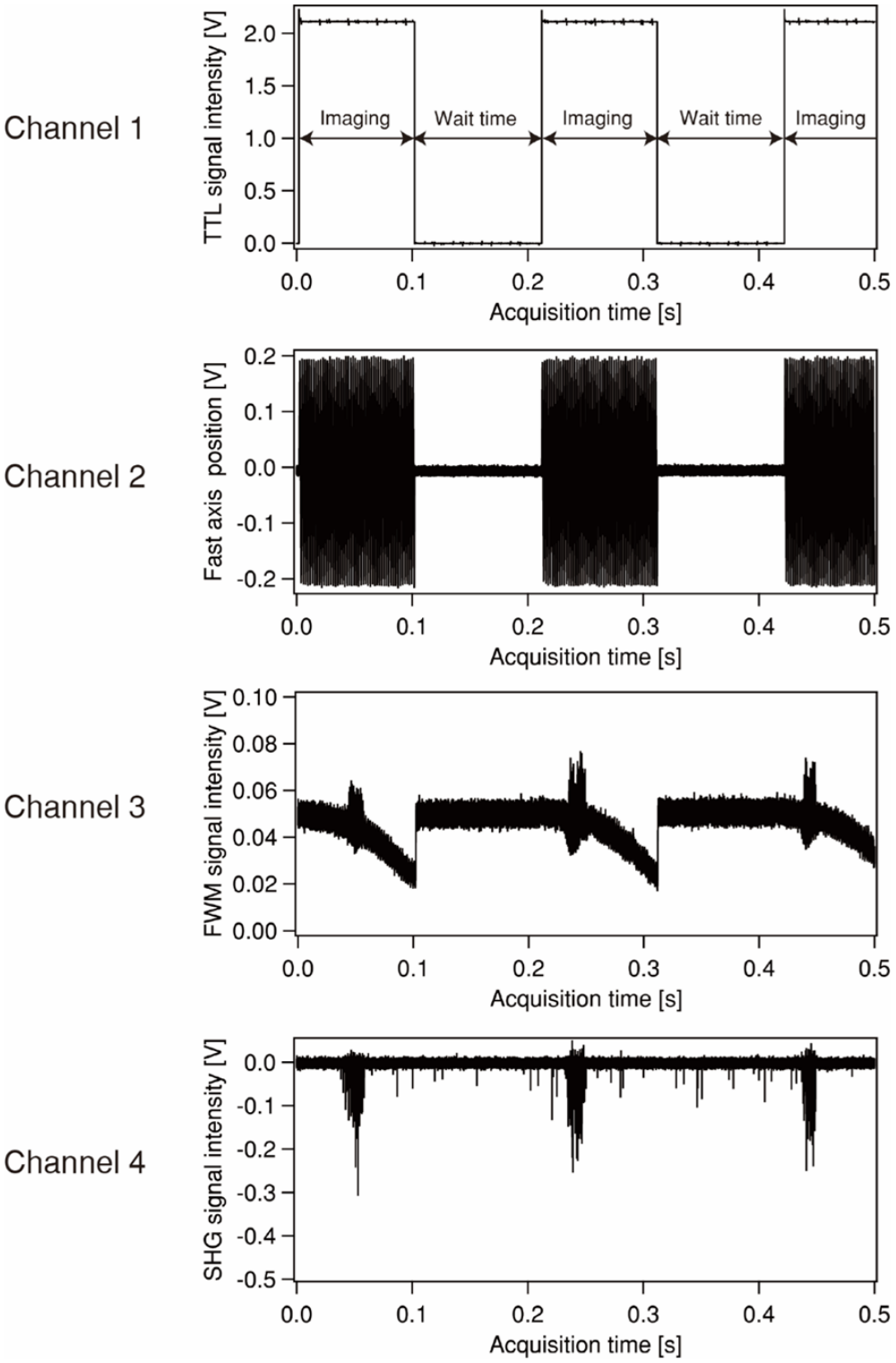

Fig. 9. Data acquisition for the construction of FWM and SHG images.

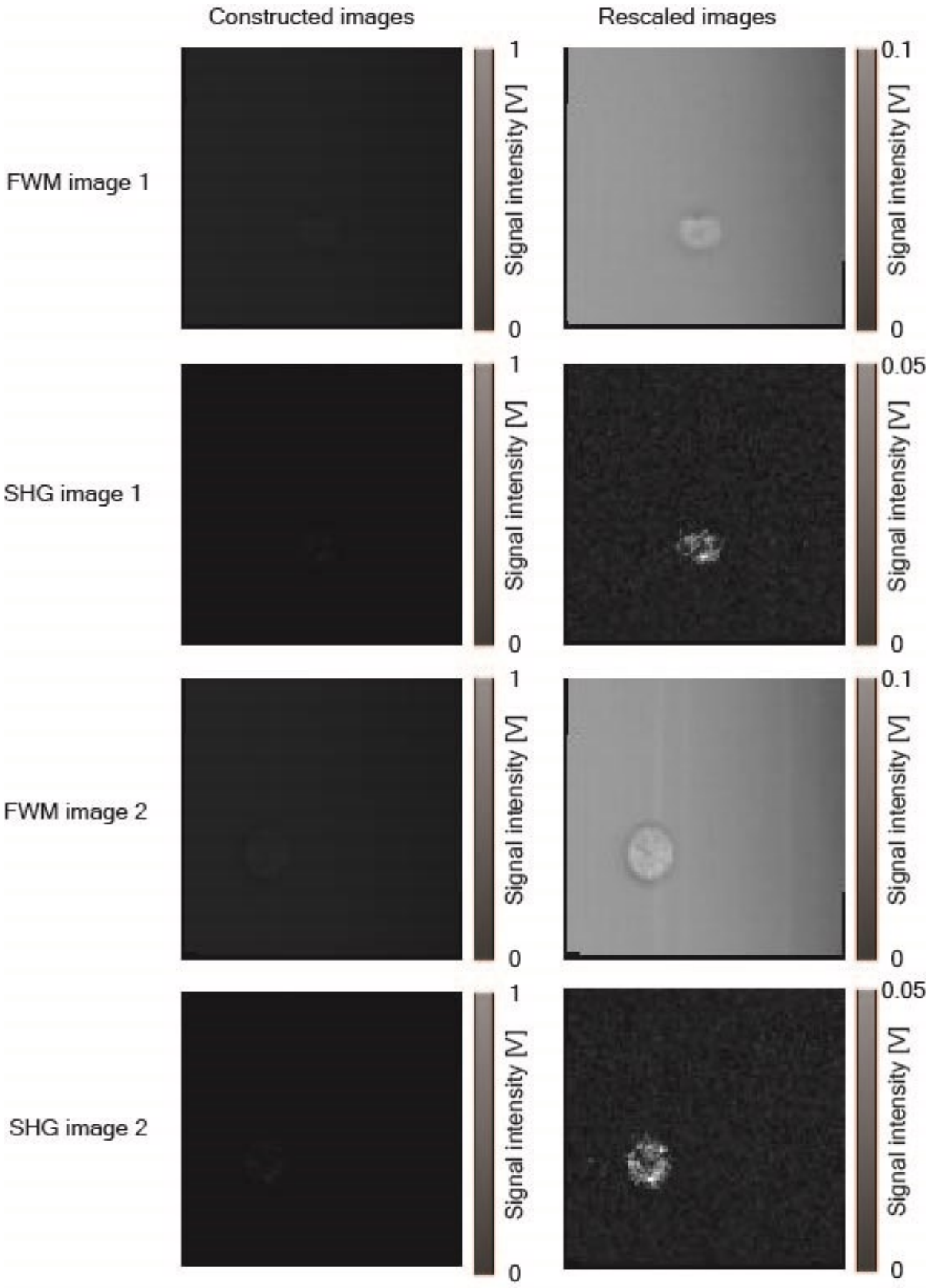

Fig. 10. Examples of generated FWM and SHG images

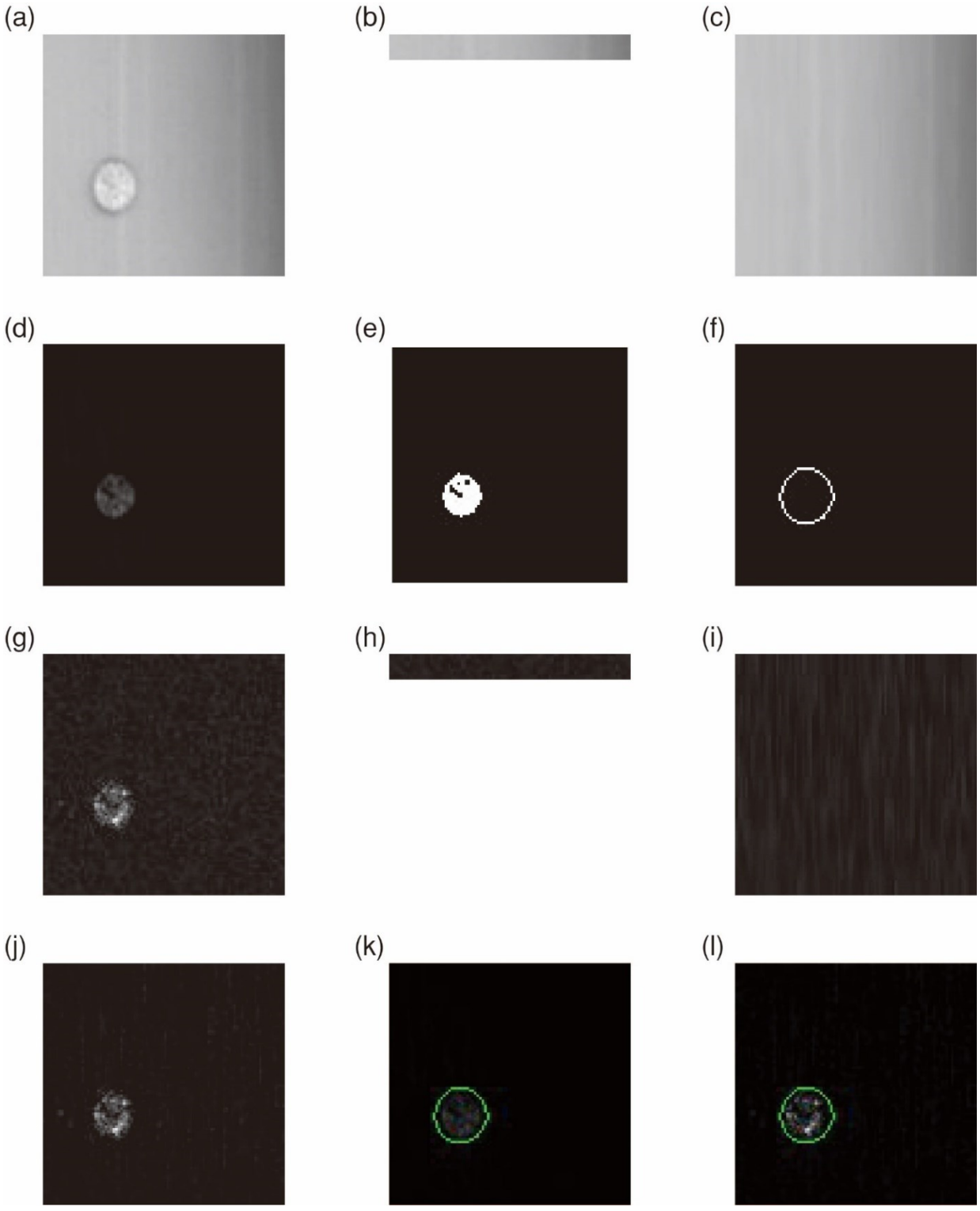

Fig. 11. FWM and SHG images analysis using *CellProfiler 4.1.3.* (a) FWM image. (b) Background cropped from the original FWM image (c) Resized background. (d) Background-free FWM image. (e) Binary image. (f) Extracted cellular outline. (g) SHG image. (h) Background cropped from SHG image. (i) A Resized background of SHG image. (j) Background-free SHG image. (k) and (l) are a FWM image overlayed with a cellular outline and an SHG image overlayed with a cellular outline, correspondingly.

3. Experimental results and discussion

3-1. SHG and FWM imaging of *Chromochloris zofingiensis* cells

To showcase the capabilities of the label-free multiphoton imaging flow cytometer I developed, I used the system for the analysis of a species of green algae, *Chromochloris zofingiensis* (NIES-2175). *C. zofingiensis* has been attracted due to its high productivity of invaluable molecules for biofuels, bioplastics, and food. There is a strong requirement to find the best cultural conditions of *C. zofingiensis* cells to boost the efficiency of their starch synthesis. In general, accumulated starch in microalgae is assessed through colorimetric analysis or Lugol staining. As a fundamental problem, nonetheless, both methods need cell fixation, pricy consumables, and lengthy procedures. Besides, the colorimetric analysis assesses the total amount of starch within cells in a bulk manner, lacking access to information on cellular heterogeneity, which is crucial for metabolism study at the cellular level. Given the current situation, I demonstrated label-free multiphoton imaging flow cytometry of *C. zofingiensis* to solve the problems above.

Fig. 12 (a) and (b) are examples of FWM and SHG images of *C. zofingiensis* cells taken by the label-free multiphoton imaging flow cytometer, correspondingly (The data processing to construct FWM and SHG images from detected nonlinear optical signals are described in section 2-3). The constructed FWM images show the cellular morphology based on $\chi^{(3)}$ mapping of intracellular molecules. By contrast, the SHG images predominantly visualize the spatial distribution of starch inside the cells. Fig. 12 (c) is the merged images of FWM images (Fig. 12 (a)) and SHG images (Fig. 12 (b)) from the identical cells, which enable the display of the relative position of starch inside of the cells. Fig. 12 (d) and (e) show an FWM and SHG image of a polystyrene bead with a diameter of 6.0-μm, accordingly. The FWM image visualizes the shape of the polystyrene beads based on its third-order nonlinear susceptibility. In contrast, no signal is seen in the SHG image because polystyrene is not a noncentrosymmetric material.

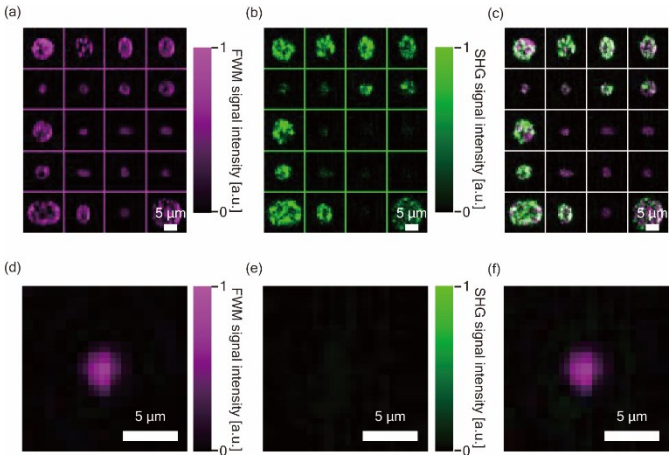

Fig. 12. FWM and SHG images taken by the label-free multiphoton imaging flow cytometer. images. (a) and (b) are constructed FWM images and SHG images of C. zofingiensis cells, correspondingly. (c) composite image of FWM and SHG images. (d) and (e) are a FWM image of a 6.0-μm polystyrene bead and a SHG image of the bead, correspondingly. (f) Composite image of FWM and SHG images.

3-2. Change in the cell size of *C. zofingiensis* cells

To present the advantage of label-free multiphoton imaging flow cytometry in being able to image a large number of single cells in sequence, I carried out imaging of *C. zofingiensis* cells to show statistically how cellular morphology changes with different medium conditions. The *C. zofingiensis* (NIES2175) cells were bought from the National Institute of Environmental Studies (Japan). The cells were precultured in a petri dish with modified acetate medium (mAC) [72] for 15 days in an incubator with an illumination cycle of light intensity of 60 μmol/m^2/s for 14 hours, followed by a 10-hour darkness. The temperature in the incubator was kept at 26 °C while preculturing and culturing the *C. zofingiensis* cells. For the culture of the cells, the medium was supplemented with glucose to reach a final concentration of 20 mg/ml. The cells are incubated in the medium with glucose for 0-9 days. The illumination condition was maintained the same as the precultured condition above. When conducting label-free multiphoton imaging flow cytometry, cultural cell media were diluted with mAC solution to be a cell concentration of 1.0 x 10^5 cells/ml and added TWEEN 20 to reach a concentration of 0.3% in order to prevent aggregation.

I carried out multiphoton imaging of the *C. zofingiensis* cells from day 0 to day 9 after the glucose supplementation with a laser power of 70 mW on the sample and a pixel duration of 10 μs (equivalent to an image capture duration of 100 ms) with the label-free imaging flow cytometer. I obtained 2,000 FWM and SHG images of *C. zofingiensis* cells for each cultural condition (See section 2-3 for detailed information on data processing to construct FWM and SHG images on *Igor 8.04* and the detail of the image analysis with *CellProfiler 4.1.3*.). Violin plots of the *C. zofingiensis* cell's area are shown in Fig. 13 (a). Violin plots are the combinations of Kernel density plots and box plots, providing visualizations of the data distributions, its probability densities, and its cumulative distributions. In a Kernel density plot, the width of the plot at different values indicates the density of the data at those values, with wider areas representing higher density (with more data points) and narrower areas representing lower density. Also, the box plot indicates 25th-75th quartiles of the data points. It is indicated that the cell size reached a maximum at around day 6 and then reduced. For comparison, I acquired bright-field images of the *C. zofingiensis* cell (Fig. 13 (b)) with a microscope (Leica MC 170 HD, Leica microsystems). As evidenced by Fig. 13 (b), the *C. zofingiensis* cell's size reached a maximum on day 6, which matches the result of the FWM images (Fig. 13 (a)). Fig. 13 (c) is a violin plot of the *C. zofingiensis* cell's area, which is calculated based on bright-field images with *CellProfiler 4.1.3*.

I performed the analysis of bright-field images of *C. zofingiensis* cells as represented in Fig. 14. Fig. 14 (a) is a bright-field image of *C. zofingiensis* cells taken with a microscope (Leica MC 170 HD, Leica

microsystems). For the calculation of cell's size from the image, I changed the original images into gray scale images using "ColorToGray" module. Following, I inverted the intensity value of each pixel of the gray scale image using the "ImageMath" module. The subsequent steps are the same as the procedures done for determining cellular outline with FWM images. Fig. 14 (f) represents the original cell image overlayed with cellular outlines (red). Even though a minor discrepancy exists between the average values of the cell areas derived from FWM and bright-field images primarily as a result of the limitation of the number of cells quantified in bright-field images, the observed similar trends between the Fig. 13 (a) and Fig 13 (c) validated that FWM imaging is reliable for the determination of the cell area.

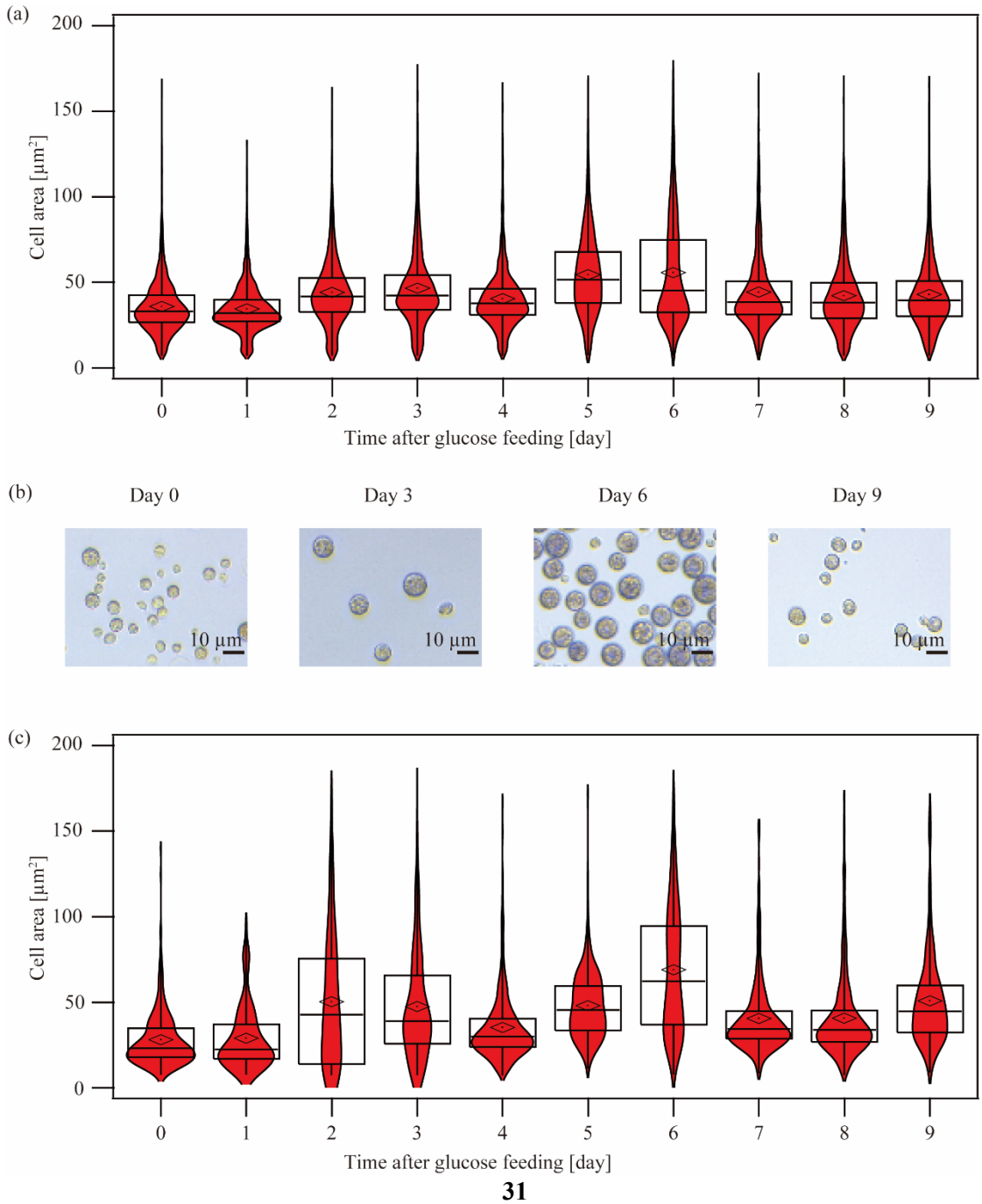

Fig. 13. Changes in *C. zofingiensis* cell size after glucose supplementation. (a) Violin plots of *C. zofingiensis* cells' areas derived from FWM images. The dots indicate mean values of cell areas. (b) *C. zofingiensis* cells bright-field images on day 0, 3, 6, and 9 days after glucose supplementation, accordingly. (c) Violin plots of *C. zofingiensis* cells' areas derived from bright-field images. The dots indicate mean values of cell areas. The box plots indicate 25th-75th quartiles of the data points.

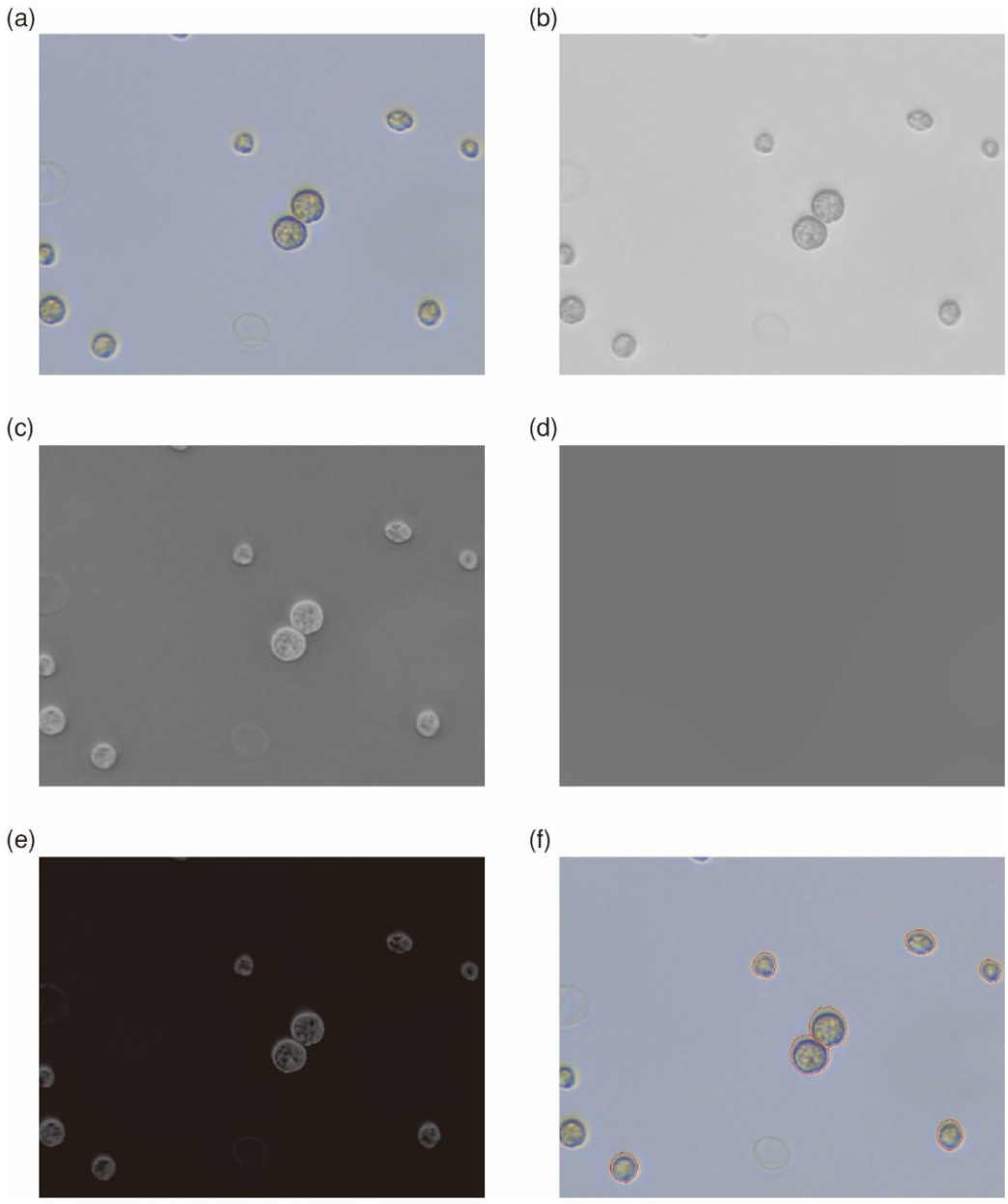

Fig. 14. *C. zofingiensis'* cellular outline determination from bright-field image. (a) Bright-field image of *C. zofingiensis* cells. (b) Gray scaled image. (c) Intensity inverted image. (d) Background. (e) Background-free image. (f) Bright-field image overlayed with cellular outlines (red).

3-3. Change in the amount of starch in *C. zofingiensis* cells

Fig. 15 (a) presents the violin plots of the sum of SHG signal intensity values on the pixels inside of the *C. zofingiensis* cells whose outlines were recognized based on the FWM images (Detailed information on the image analysis was described in section 2-3). The sum of SHG signal intensity values reached a maximum on day 6. To verify that the accumulated starch is the source of the SHG signal, I took bright-field images of the *C. zofingiensis* cells stained with a Lugol's solution (iodine-potassium iodide solution). Regarding the Lugol staining, I followed the standard protocol for Lugol staining of intracellular starch [60]. The *C. zofingiensis* cells were fixed with 2.5% of glutaraldehyde for 10 mins. After the cell fixation, the cells were washed three times and then kept in Dulbecco's phosphate-buffered saline (DPBS) in a refrigerator at 4 °C until the Lugol staining imaging experiment. In the process of Lugol staining, I added Lugol solution (5% of I^2 / 10% of KI) into the fixed cells solution to be a final concentration of 2% of I^2 and 4% of KI, respectively. Then, the cells with Lugol solution were incubated for 10 mins. The *C. zofingiensis* cell imaging with Lugol staining was performed with a microscope (Leica MC 170 HD, Leica microsystems) with a 40x magnification objective lens. In regard to the Lugol-stained image analysis, in the same manner as the analysis of the bright-field images of *C. zofingiensis* cells, I extracted cellular outlines. Fig. 16 (a) is an image of *C. zofingiensis* cells stained with Lugol. The original image was changed into a gray scale using "ColorToGray" module (Fig. 16 (b)). Next, each intensity value on the pixels of the gray scaled image was inverted using the "ImageMath" module. The subsequent steps are the same as the procedures done for determining cellular outline with FWM images. Fig. 16 (f) represents the original Lugol-stained image overlayed with cellular outlines (red). The total values of Lugol intensity inside of cells were computed using the "MeasureObjectIntensity" module. The images of *C. zofingiensis* cells (Day 0, 3, 6, and 9 after glucose supplementation) stained with Lugol are displayed in Fig. 15 (b). In the images, the iodine-starch interaction turned the color of starch in the cells blue-black [60]. As evidenced by Fig. 15 (b), the amount of accumulated starch in the *C. zofingiensis* cells reached a maximum on day 6, which is consistent with the result acquired from SHG images (Fig. 15 (a)). For further quantitative analysis, I constructed violin plots of the amount of accumulated starch in the *C. zofingiensis* cells based on the bright-field images of the cells stained with Lugol (Fig. 15 (c)). The similarities seen in Fig.15 (a) and Fig. 15 (b) validate that SHG imaging primarily visualizes the intracellular starch molecules. This capability of SHG imaging flow cytometry to visualize non-centrosymmetric materials inside of cells in succession greatly expands the applicability of label-free imaging flow cytometry.

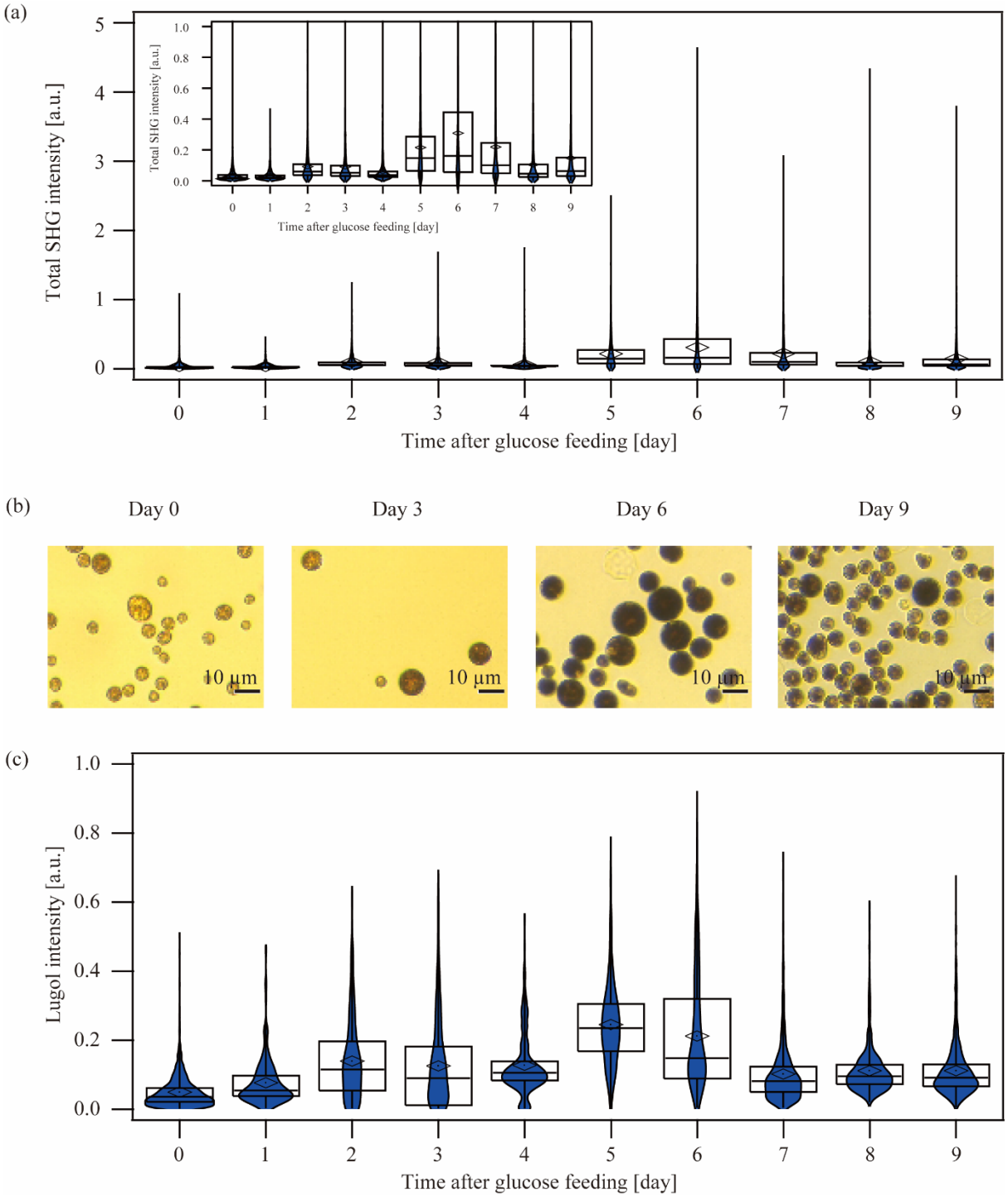

Fig. 15. Change in the amount of starch in *C. zofingiensis* cells after glucose supplementation. (a) Violin plots of the sum of the SHG signal intensity from *C. zofingiensis* cells. The dots indicate mean values of the sum of the SHG signal intensity. (b) Bright-field images of *C.* zofingiensis cells stained with Lugol (day 0, 3, 6, and 9 after glucose supplementation, correspondingly). (c) Violin plots of the sum of Lugol intensity from *C. zofingiensis* cells. The dots indicate mean values of the sum of the Lugol intensity. The box plots indicate 25th-75th quartiles of the data points.

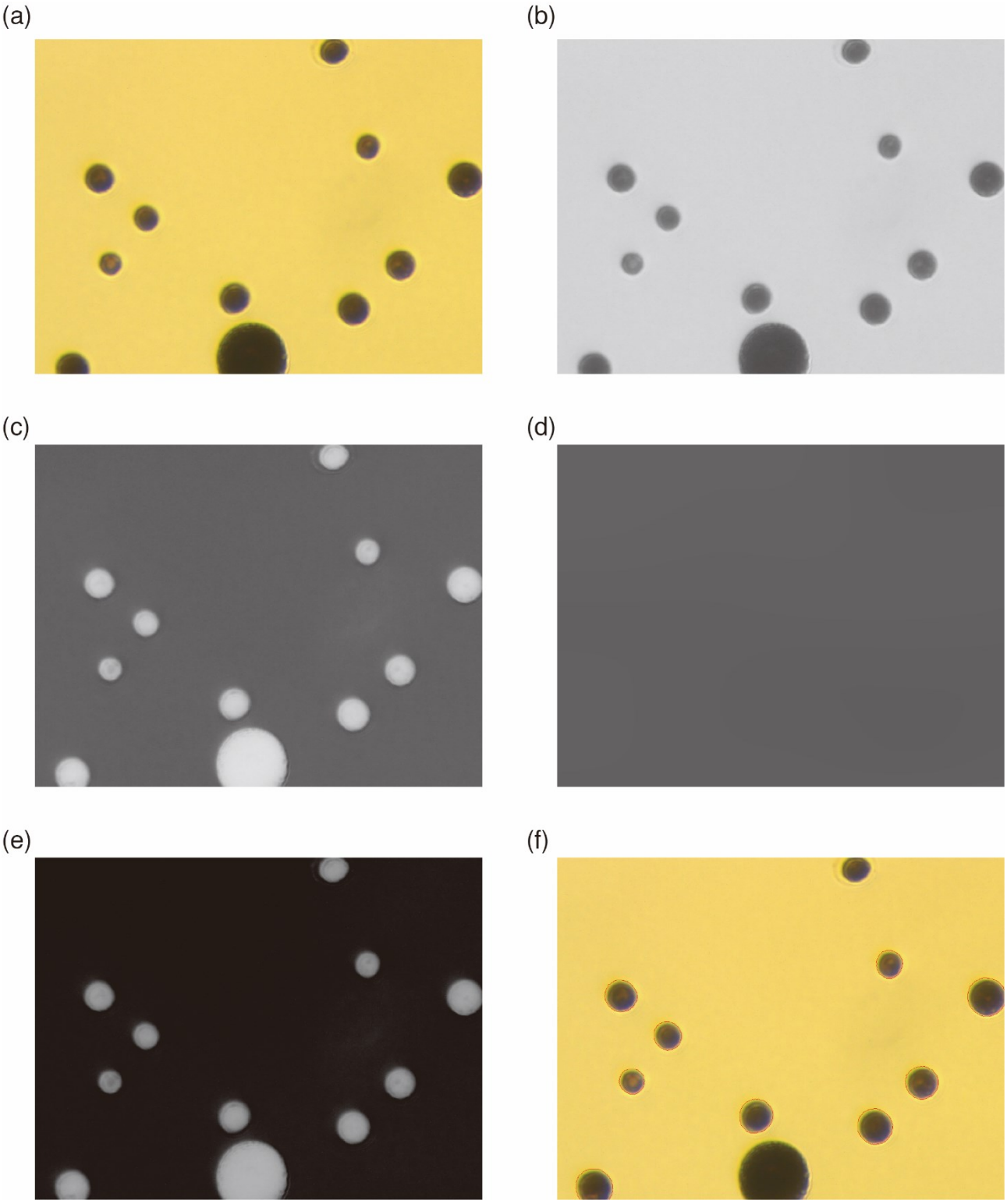

Fig. 16. Lugol-stained *C. zofingiensis* cells image analysis on *CellProfiler4.1.3*. (a) Bright-field image of Lugol-stained *C. zofingiensis* cells. (b) Gray scaled image. (c) Intensity inverted image. (d) Background. (e) Background-free image. (f) Bright-field image overlayed with cellular outlines (red).

3-4. Change in the spatial distribution of starch in *C. zofingiensis* cells

To better understand the morphogenesis of *C. zofingiensis,* I performed the FWM and SHG image analysis to see how the spatial distribution of starch accumulated in *C. zofingiensis* cells changes after glucose supplementation. The scatter plots of "the fraction of SHG intensity" and the *C. zofingiensis* cell size in Fig. 17. "The fraction of SHG intensity" was computed by using the "MeasureObjectIntensityDistribution" module on *CellProfiler 4.1.3*. As a first step in this process, Each *C. zofingiensis* cell visualized by FWM imaging was split into the inner bin (bin 1) and the outer bin (bin 2). Next, the sum of SHG signal intensities in each bin was computed to derive "the fraction of SHG intensity" in bin 1 (Fig. 18).

The scatter plots for day 0 and day 1 are well represented as a single population, which means that the cell cycles of *C. zofingiensis* cells are noticeably uniform after the preculture. From day 2, each scatterplot shows two populations, corresponding to mature cells (> 60 μm^2) and daughter cells (< 60 μm^2). The former population (> 60 μm^2) has a smaller value of SHG fraction in bin 1 (which indicates that starch exists more uniformly inside of the cells), whilst the latter population (< 60 μm^2) has a larger value of SHG fraction in bin 1 (which indicates that starch is more localized around the center of the cells). Additionally, an anti-correlation between the SHG fraction and the cell size is observed among the mature cells (cell population with a larger cell size). (This anti-correlation is clearly seen on the scatter plot for day 6). The observed anti-correlation is accounted for by the hypothesis by Fučíková *et al.* that more mature cells have multiple parental chloroplasts while younger cells contain just a single chloroplast [73]. There is another noteworthy finding on the scatter plots, which is that the cell population of daughter cells is shifted to Q4 (higher SHG fraction in bin 1) on day 6 and day 7. This shift indicates that if mature cells were divided into daughter cells on day 5 and day 6, the accumulated starch was more concentrated around the center of the daughter cells, suggesting that the starch in the daughter cells is more centrally localized in the case that they are divided from the parental cells possessing more numerous (4, 8, and 16) nuclei rather than divided from the parental cells with 2 nuclei [74].

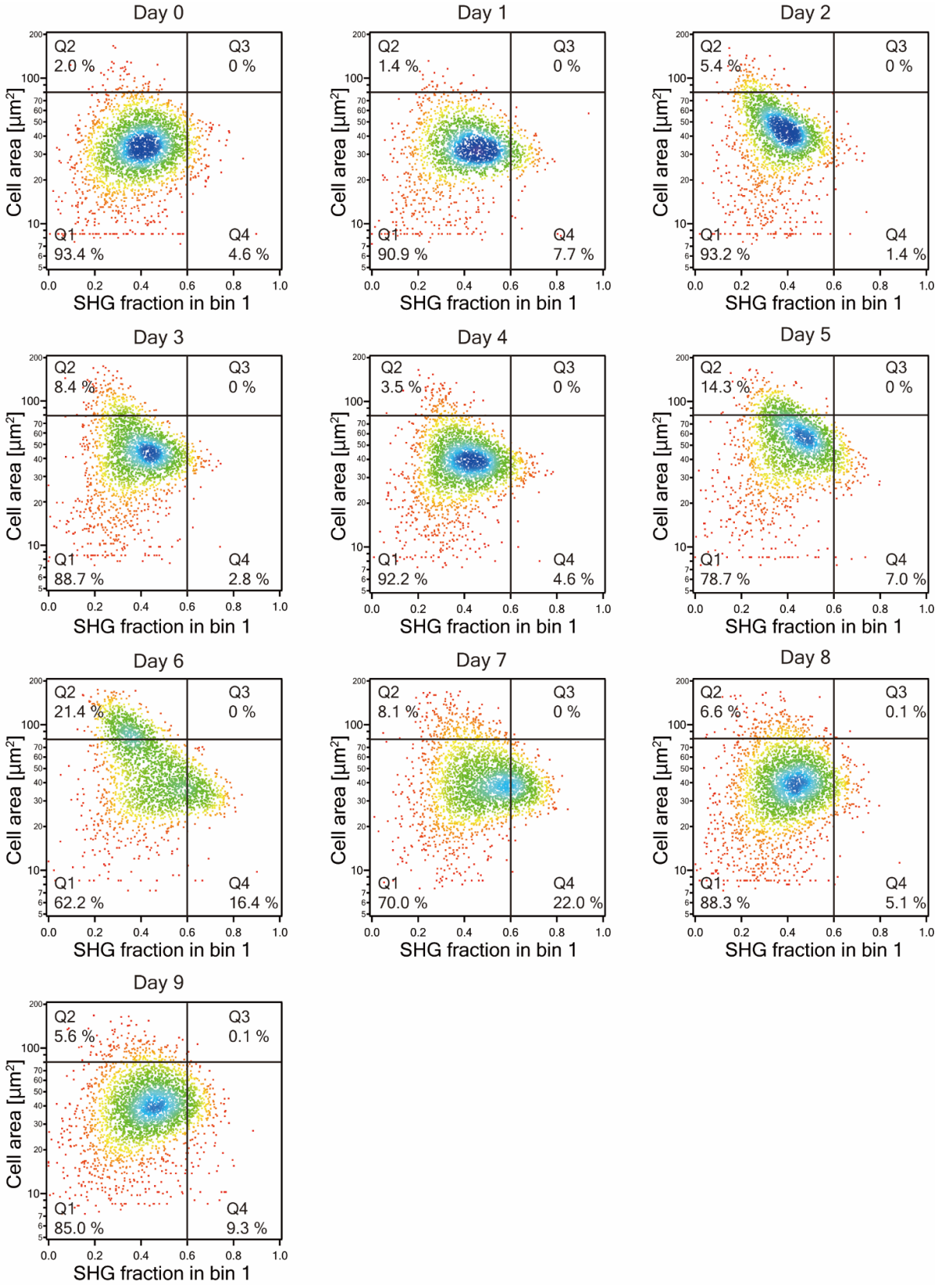

Fig. 17. Scatter plots of SHG fraction v.s. the cell area of *C. zofingiensis* cells from day 0 to day 9 after glucose supplementation.

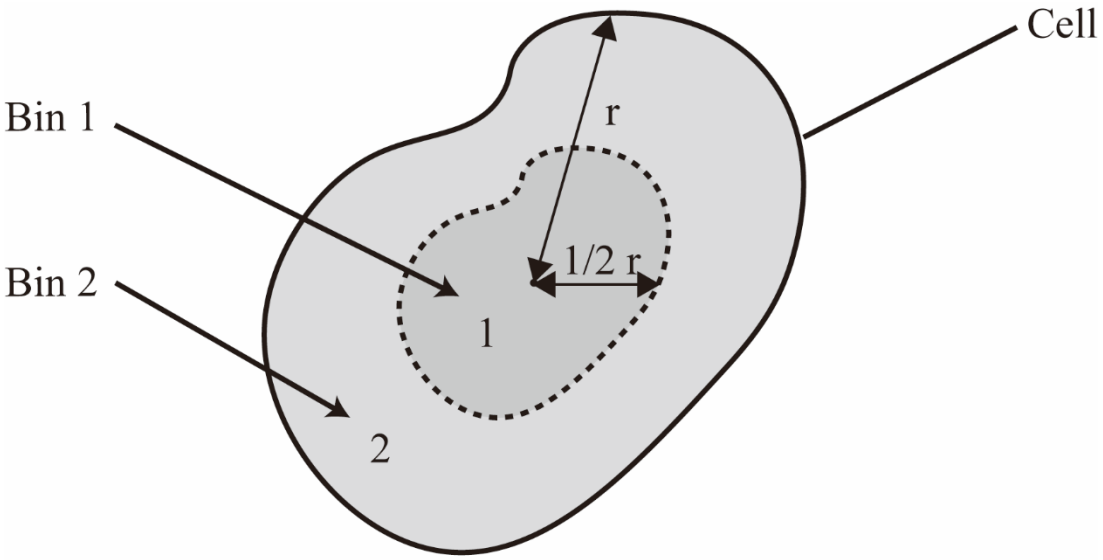

Fig. 18. Schematical image of the cell binning.

3-5. Discussion

In section 3-1, first, I demonstrated the visualization of cellular morphology and noncentrosymmetric material by FWM images and SHG images with the label-free multiphoton imaging flow cytometer that I developed. As well as it was obvious from the standard bright-field microscopic images that *C. zofingiensis* shows heterogeneity with respect to cell size, the results of this section indicated that the amount and distribution of starch stored in the cells also varies from cell to cell. In this first demonstration of flow cytometry, I performed the imaging of *C. zofingiensis* cells. Because it is known that SHG is also sensitive to other noncentrosymmetric materials such as collagen, as well as SHG tag, the label-free imaging flow cytometry has great potential for other applications such as the imaging of transformations of extracellular matrix (ECM) of spheroid cells [75] and stem cells tagged with nanocrystal SHG tags [52]. Although the size of the multiphoton image and the pixel resolution are set as 50 x 50 μm^2 and 100 x 100 pixels, respectively, during all the measurements with the label-free multiphoton imaging flow cytometer in this thesis, both the image size and the pixel resolution in the multiphoton imaging flow cytometry can be optimized for the size of the measurement objects by controlling the amplitude and the frequency of the 2D-galvanometric scanners.

Next, the capability of the label-free imaging flow cytometry to determine cell sizes based on FWM imaging was demonstrated in section 3-2. The changes in *C. zofingiensis* cell sizes were caused by the cells' asexual reproduction processes with three phases (growth, ripening, and cell division), and the change could be observed by the developed label-free imaging flow cytometer and validated by the bright-field imaging. This label-free imaging flow cytometer holds the advantage that the cellular morphological information can be obtained via FWM with the same pulse laser source for SHG imaging without any additional light source or expensive high-speed camera. For a potential upgrade of the label-free multiphoton imaging flow cytometer, electric-resonant FWM imaging can be executed with higher sensitivity (around 50 molecules) [55] using a wavelength-tunable pulsed laser. Moreover, by integrating a Michelson interferometer into the label-free multiphoton imaging flow cytometer, it becomes feasible to carry out Fourier-transform coherent anti-Stokes Raman scattering (FT-CARS) imaging, a technique I have demonstrated in the previous work [76]. FT-CARS allows for the acquisition of vibrational information from intracellular molecules in a label-free manner. Besides, Mahou *et al.* demonstrated FWM and third-harmonic generation (THG) "microscopy", which enables the acquisition of additional structural information by the $\boldsymbol{\chi^{(3)}}$ mapping via FWM and visualizing the distribution of $\boldsymbol{\Delta\chi^{(3)}}$ [53]. It is possible that the capability of THG imaging is integrated into the label-free

"imaging flow cytometry" by using a collection lens that has high transparency for both NIR (FWM signal) and UV (THG signal), a sensitive photodetector for UV and band-pass filters for THG signal.

In section 3-3, I demonstrated that the label-free imaging flow cytometry can selectively visualize accumulated starch in *C. zofingiensis* cells. According to the obtained results of the changes in cell size and the amount of starch, it is suggested that the growing phase continued for around 5 days, and then starch was synthesized around day 6 intensively. This SHG imaging flow cytometry solved the problems of the conventional method using Lugol, such as its requirement of cell fixation, time-consuming protocol, and the effect of intracellular molecules other than starch, such as carotenoids and chlorophyll in bright-field imaging (See Fig. 14 (b) for bright-field images of *C. zofingiensis* cells without Lugol-staining). During the Q&A session of my preliminary report presentation, I was asked if SHG imaging cannot distinguish between starch and collagen when both are present at the same time, which is correct. This is because the label-free multiphoton imaging flow cytometry visualizes noncentrosymmetric materials based on $|\boldsymbol{\chi}^{(2)}|$ by SHG imaging. In future applications, if there are situations where multiple types of noncentrosymmetric materials such as starch, collagen, and myosin exist inside of a single cell, the technique of polarization-resolved SHG (pSHG) [77] would be integrated into the multiphoton imaging flow cytometry, which enables to analyze elements of $\boldsymbol{\chi}^{(2)}$ tensor for distinguishing such noncentrosymmetric materials. As the most important demonstration, finally, I performed the analysis of the evolution of the spatial distribution of accumulated starch in *C. zofingiensis* cells. On the acquired scatter plots based on 2,000 FWM and SHG images for each 10 cultural conditions, it was observed that the cell population began to divide into two populations from day 2, that starch is more delocalized in the larger cells (mature cells), and that starch is more centrally localized in the newly divided daughter cells on day 6 and day 7. Conventional methods utilized in cellular morphogenesis studies [78–81] are limited in their capabilities to perform statistically significant analyses. I believe that further statistical microbiological studies using the label-free imaging flow cytometer will contribute to more comprehensive understandings of the metabolic system of *C. zofingiensis,* including how the chloroplast-driven photosynthesis and mitochondrial glucose metabolism are interacted and regulated [82]. As a possibility of the upgrade of the label-free imaging flow cytometer, the introduction of the cell sorting system [24] to the label-free imaging flow cytometer, sorting cells based on information obtained from the resulting FWM and SHG images and then examining the correlations between phenotypes and genetic mutations observed by genetic analysis, is expected to have great potential for medical and microbiological studies, as well as industrial applications such as developing more productive cell lines.

4. Summary and outlook

In this Ph.D. thesis, I developed a new label-free imaging flow cytometry named label-free multiphoton imaging flow cytometry for high-throughput imaging of noncentrosymmetric materials in living cells [49]. The developed multi-photon imaging flow cytometer is based on nonlinear optical imaging of FWM and SHG, which provides cellular morphological information and the spatial distribution of intracellular noncentrosymmetric materials. The label-free imaging flow cytometer consists of a microfluidic system, a dual color (FWM and SHG) imaging system with a 2D-scanning beam, and a fast signal acquisition circuit designed for simultaneous detection of FWM and SHG images of flowing cells in the flow cytometer. Consequently, the label-free imaging flow cytometer provides FWM and SHG images with a pixel resolution of 100 × 100 pixels, a spatial resolution of 500 nm, a field of view of 50 μm × 50 μm, and an intensity depth of 14-bit at a high event rate of 4 - 5 eps.

As the demonstration of the label-free imaging flow cytometry, I performed multiphoton imaging of *C. zofingiensis* cells, which is known as a highly effective producer of valuable materials for bioplastic, biofuel, and food. I carried out multiphoton imaging of the *C. zofingiensis* cells from day 0 to day 9 after glucose supplementation into the culture media. From the acquired FWM images, it is observed that the *C. zofingiensis* cells reached maximum sizes at around day 6, which was validated by the comparison of the result from bright-field images. Next, the change in the amount of accumulated starch in the *C. zofingiensis* cells from day 0 to day 9 was obtained from the SHG images (visualization of starch) and FWM images (visualization of cellular outline). It was found that the amount of starch accumulated in the cell reached a maximum at around day 6, which is consistent with the result obtained from Lugol-staining imaging. As the most important demonstration, lastly, I performed the analysis of how the spatial distribution of accumulated starch changed from day 0 to day 9. From the scatter plots based on 2,000 FWM and SHG images for every 10 conditions, it was observed that starch was more evenly present in larger mature cells, which is accounted for by the more mature cells holding a larger number of chloroplasts. Another noteworthy finding was the starch was more centrally localized in the daughter cells on day 6 and day 7, which implies that the starch was more localized if they were newly divided from larger parental cells. Conventional methods used in cellular morphogenesis studies have limitations in the capability of performing statistically significant image analysis. The newly developed label-free multiphoton imaging flow cytometry solved the problem, and it paves the way for further statistical microbiological studies, including the metabolic analysis of the interaction of chloroplast-driven photosynthesis and mitochondrial glucose metabolism in microbiological cells.

References

1. Mckinnon, K. M. Flow cytometry : an overview. *Curr. Protoc. Immunol.* 120, 1–5 (2018).
2. Adan, A. *et al.* Flow cytometry : basic principles and applications. *Crit. Rev. Biotechnol.* 37, 163–176 (2017).
3. Jahan-Tigh, R. R. *et al.* Flow cytometry. *J. Invest. Dermatol.* 132, e1 (2012).
4. Perfetto, S. P. *et al.* Seventeen-colour flow cytometry : unravelling the immune system. *Nat. Rev. Immunol.* 4, 648-655 (2004).
5. Rieseberg, M. *et al.* Flow cytometry in biotechnology. *Appl. Microbiol. Biotechnol.* 56, 350–360 (2001).
6. Baumgarth, N. *et al.* A practical approach to multicolor flow cytometry for immunophenotyping. *J. Immunol. Methods* 243, 77–97 (2000).
7. Bariogie, B. *et al.* Flow cytometry in clinical cancer research. *Cancer Res.* 43, 3982–3997 (1983).
8. Mousset, C. M. *et al.* Comprehensive phenotyping of T cells using flow cytometry. *Cytom. Part A* 95, 647–654 (2019).
9. Robinson, J. P. Wallace H . Coulter : decades of invention and discovery. *Cytom. Part A* 83, 424–438 (2013).
10. Simson, E. Wallace Coulter's life and his impact on the world. *Int. J. Lab. Hematol.* 35, 230–236 (2013).
11. Mattern, C. F. *et al.* Determination of number and size of particles by electrical gating. *J. Appl. Physiol.* 10, 56–70 (1957).
12. Fulwyler, M. J. Electronic separation of biological cells by volume. *Sci.* 150, 910–911 (1965).
13. Herzenberg, L. A. *et al.* Fluorescence-activated cell sorting. *Sci. Am.* 234, 108–118 (1976).
14. Wei, D. *et al.* Visualizing interactions of circulating tumor cell and dendritic cell in the blood circulation using in vivo imaging flow cytometry. *IEEE Trans. Biomed. Eng.* 66, 2521–2526 (2019).
15. Holzner, G. *et al.* High-throughput multiparametric imaging flow cytometry: toward diffraction-limited sub-cellular detection and monitoring of sub-cellular processes. *Cell Rep.* 34, 108824 (2021).
16. Miura, T. *et al.* On-chip light-sheet fluorescence imaging flow cytometry at a high flow speed of 1 m/s. *Biomed. Opt. Express* 9, 3424-3433 (2018).
17. Matsumura, H. *et al.* Virtual-freezing fluorescence imaging flow cytometry with 5-aminolevulinic acid stimulation and antibody labeling for detecting all forms of circulating tumor cells. *Lab Chip* 23, 1561–1575 (2023).
18. Huang, K. *et al.* Deep imaging flow cytometry. *Lab Chip* 22, 876–889 (2022).
19. Wu, J. *et al.* A light sheet based high throughput 3D-imaging flow cytometer for phytoplankton analysis. *Opt. Express* 21, 14474-14480 (2013).
20. Görgens, A. *et al.* Optimisation of imaging flow cytometry for the analysis of single extracellular vesicles by using fluorescence-tagged vesicles as biological reference material. *J. Extracell. Vesicles* 8,

1587567 (2019).

21. Mikami, H. *et al.* Ultrafast confocal fluorescence microscopy beyond the fluorescence lifetime limit. *Optica* 5, 117-126 (2018).
22. Diebold, E. *et al.* Digitally synthesized beat frequency multiplexing for sub-millisecond fluorescence microscopy. *Nat. Photonics* 7, 806–810 (2013).
23. Harmon, J. *et al.* Accurate classification of microalgae by intelligent frequency-division-multiplexed fluorescence imaging flow cytometry. *OSA Contin.* 3, 430-440 (2020).
24. Nitta, N. *et al.* Intelligent image-activated cell sorting. *Cell* 175, 266-276 (2018).
25. Wei, D. *et al.* Visualizing interactions of circulating tumor cell and dendritic cell in the blood circulation using in vivo imaging flow cytometry. *IEEE Trans. Biomed.* 66, 2521-2526 (2019).
26. Cerrato, G. *et al.*Quantitative determination of phagocytosis by bone marrow-derived dendritic cells via imaging flow cytometry. *Meth. Enzymol.* 632, 27-37 (2020).
27. Gordon, S. Phagocytosis: an immunobiologic process. *Immunol. Rev.* 44, 463–475 (2016).
28. Park, Y. *et al.* Imaging flow cytometry protocols for examining phagocytosis of microplastics and bioparticles by immune cells of aquatic animals. *Front. Immunol.* 11, 203 (2020).
29. Tertel, Tobias *et al.* Analysis of individual extracellular vesicles by imaging flow cytometry. *Meth. Enzymol.* 645, 55-78 (2020).
30. Yáñez-Mó, M. *et al.* Biological properties of extracellular vesicles and their physiological functions. *J. Extracell. Vesicles* 4, 27066 (2015).
31. Lener, T. *et al.* Applying extracellular vesicles based therapeutics in clinical trials - an ISEV position paper. *J. Extracell. Vesicles* 4, 30087 (2015).
32. Article, O. A new microparticle size calibration standard for use in measuring smaller microparticles using a new flow cytometer. *J. Thromb. Haemost.* 9, 1216–1224 (2011).
33. Payes, C. *et al.* Cell interaction analysis by imaging flow cytometry. *IntechOpen, London, UK* 303–322 (2012).
34. Blasi, T. *et al.* Label-free cell cycle analysis for high-throughput imaging flow cytometry. *Nat. Commun.* 7, 10256 (2016).
35. Filby, A. *et al.* An Imaging flow cytometric method for measuring cell division history and molecular symmetry during mitosis. *Cytom. Part A* 79, 496–506 (2011).
36. Jensen, E. C. Use of fluorescent probes: their effect on cell biology and limitations. *Anat. Rec.* 295, 2031–2036 (2012).
37. Lei, C. *et al.* High-throughput imaging flow cytometry by optofluidic time-stretch microscopy. *Nat. Protoc.* 13, 1603–1631 (2018).
38. Lau, A. K. S. *et al.* Optofluidic time-stretch imaging-an emerging tool for high-throughput imaging

flow cytometry. *Lab Chip* 16, 1743–1756 (2016).

39. Kobayashi, H. *et al.* Intelligent whole-blood imaging flow cytometry for simple, rapid, and cost-effective drug-susceptibility testing of leukemia. *Lab Chip* 19, 2688–2698 (2019).
40. Kobayashi, H. *et al.* Label-free detection of cellular drug responses by high-throughput bright-field imaging and machine learning. *Sci. Rep.* 7, 1–9 (2017).
41. Jiang, Y. *et al.* Label-free detection of aggregated platelets in blood by machine-learning-aided optofluidic time-stretch microscopy. *Lab Chip* 17, 2426–2434 (2017).
42. Zhou, Y. *et al.* Intelligent classification of platelet aggregates by agonist type. *Elife* 9, e52938 (2020)
43. Weng, Y. *et al.* Typing of acute leukemia by intelligent optical time-stretch imaging flow cytometry on a chip. *Lab Chip* 23, 1703–1712 (2023).
44. Suzuki, Y. *et al.* Label-free chemical imaging flow cytometry by high-speed multicolor stimulated Raman scattering. *Proc. Natl. Acad. Sci. U. S. A.* 116, 15842–15848 (2019).
45. Zong, C. *et al.* Plasmon-enhanced stimulated Raman scattering microscopy with single-molecule detection sensitivity. *Nat. Commun.* 10, 5318 (2019).
46. Ba, C., Shain, *et al.* High-throughput label-free flow cytometry based on matched-filter compressive imaging. *Biomed. Opt. Express* 9, 6145-6153 (2018).
47. Rane, A. S. *et al.* High-throughput multi-parametric imaging flow cytometry. *Chem* 3, 588–602 (2017).
48. Blasi, T. *et al.* Label-free cell cycle analysis for high-throughput imaging flow cytometry. *Nat. Commun.* 7, 10256 (2016).
49. Kinegawa, R. *et al.* Label-free multiphoton imaging flow cytometry. *Cytom. Part A* 103, 584–592 (2023).
50. Brackmann, C. *et al.* Visualization of β-carotene and starch granules in plant cells using CARS and SHG microscopy. *J. Raman Spectrosc.* 42, 586–592 (2011).
51. Nadiarnykh, O. *et al.* Alterations of the extracellular matrix in ovarian cancer studied by Second Harmonic Generation imaging microscopy. *BMC Cancer* 10, 1–14 (2010).
52. Sugiyama, N. *et al.* Effective labeling of primary somatic stem cells with BaTiO3 nanocrystals for second harmonic generation imaging. *Small* 14, 1703386 (2018).
53. Mahou, P. *et al.* Combined third-harmonic generation and four-wave mixing microscopy of tissues and embryos. *Biomed. Opt. Express* 2, 2837-2849 (2011).
54. Wang, Y. *et al.* Four-wave mixing microscopy of nanostructures. *Adv. Opt. Photonics* 3, 1–52 (2011).
55. Min, W. *et al.* Near-degenerate four-wave-mixing microscopy. *Nano Lett.* 9, 2423–2426 (2009).
56. Cinar, S. O. *et al.* Bioplastic production from microalgae: a review. *Int. J. Environ. Res. Public Health* 17, 3842 (2020).
57. Rumin, J. *et al.* Analysis of scientific research driving microalgae market opportunities in Europe. *Mar.*

Drugs 18, 264 (2020).

58. Varfolomeev, S. D. *et al.* Microalgae as source of biofuel, food, fodder, and medicines. *Appl. Biochem. Microbiol.* 47, 789–807 (2011).
59. Gifuni, I. *et al.* Microalgae as new sources of starch: Isolation and characterization of microalgal starch granules. *Chem. Eng. Trans.* 57, 1423–1428 (2017).
60. Takeshita, T. *et al.* A simple method for measuring the starch and lipid contents in the cell of microalgae. *Cytologia.* 80, 475–481 (2015).
61. Fernandes, B. *et al.* Starch determination in Chlorella vulgaris-a comparison between acid and enzymatic methods. *J. Appl. Phycol.* 24, 1203–1208 (2012).
62. Campagnola, P. J. *et al.* Second-harmonic imaging microscopy of living cells. *J. Biomed. Opt.* 6, 277-286 (2001).
63. Mohler, W. *et al.* Second harmonic generation imaging of endogenous structural proteins. *Methods* 29, 97–109 (2003).
64. Mazumder, N. *et al.* Label-free non-linear multimodal optical microscopy — basics, development, and applications. *Front. Phys.* 7, 1–26 (2019).
65. Rivard, M. *et al.* Imaging the bipolarity of myosin filaments with interferometric second harmonic generation microscopy. *Biomed. Opt. Express* 4, 2078-2086 (2013).
66. Zipfel, W. R. *et al.* Live tissue intrinsic emission microscopy using multiphoton-excited native fluorescence and second harmonic generation. *Proc. Natl. Acad. Sci. U. S. A.* 100, 7075–7080 (2003).
67. Ehmke, T. *et al.* Spectral behavior of second harmonic signals from organic and non-organic materials in multiphoton microscopy. *AIP Adv.* 5, 084903 (2015).
68. Zipfel, W. R., Williams, R. M. & Webb, W. W. Nonlinear magic: Multiphoton microscopy in the biosciences. *Nat. Biotechnol.* 21, 1369–1377 (2003).
69. Garrett, N. *et al.* Imaging the uptake of gold nanoshells in live cells using plasmon resonance enhanced four wave mixing microscopy. *Opt. Express* 19, 17563–17574 (2014).
70. Lindley, M. *et al.* Highly sensitive Fourier-transform coherent anti-Stokes Raman scattering spectroscopy via genetic algorithm pulse shaping. *Opt. Lett.* 46, 4320-4323 (2021).
71. Piyasena, M. E. *et al.* Multinode acoustic focusing for parallel flow cytometry. *Anal. Chem.* 84, 1831–1839 (2012).
72. Nozaki, H. *et al.* Morphology and paedogamous sexual reproduction in Chlorogonium capillatum sp. nov.(Volvocales, Chlorophyta). *J. Phycol.* 31, 655–663 (1995).
73. Fučíková, K. *et al.* Intersection of Chlorella, Muriella and Bracteacoccus: resurrecting the genus Chromochloris Kol et Chodat (Chlorophyceae, Chlorophyta). *Fottea* 12, 83–93 (2012).
74. Koren, I. *et al.* Chromochloris zofingiensis (Chlorophyceae) divides by consecutive multiple fission

cell-cycle under batch and continuous cultivation. *Biology* 10, 157 (2021).

75. Bourn, M. D. *et al.* High-throughput microfluidics for evaluating microbubble enhanced delivery of cancer therapeutics in spheroid cultures. *J. Control. Release* 326, 13–24 (2020).
76. Kinegawa, R. *et al.* High-speed broadband Fourier-transform coherent anti-Stokes Raman scattering spectral microscopy. *J. Raman Spectrosc.* 50, 1141–1146 (2019).
77. Amat-Roldan, I. *et al.* Fast image analysis in polarization shg microscopy. *Opt. Express* 18, 17209-17219 (2010).
78. Liu, J. *et al.* Chlorella zofingiensis as an alternative microalgal producer of astaxanthin: biology and industrial potential. *Mar. Drugs* 12, 3487–3515 (2014).
79. Azaman, S. N. A. *et al.* A comparison of the morphological and biochemical characteristics of chlorella sorokiniana and chlorella zofingiensis cultured under photoautotrophic and mixotrophic conditions. *PeerJ* 5, e3473 (2017).
80. Zhang, Z. *et al.* Glucose triggers cell structure changes and regulates astaxanthin biosynthesis in Chromochloris zofingiensis. *Algal Res.* 39, 101455 (2019).
81. Zhang, Z. *et al.* Chloroplast morphogenesis in Chromochloris zofingiensis in the dark. *Algal Res.* 45, 101742 (2020).
82. Zhang, Z. *et al.* Investigation of carbon and energy metabolic mechanism of mixotrophy in Chromochloris zofingiensis. *Biotechnol. Biofuels* 14, 1–16 (2021).

Appendix

Appendix. 1. *Igor* code used for construction of FWM and SHG images from acquired signals.

```
TwoDimensionalPlots(pixsize)#pragma TextEncoding = "UTF-8"
#pragma rtGlovals=3
w=1functon autoloadwave()
MultiThreadingcontrol setMode=8
GBLoadWave/O/B/T={4,4}/w=1 /n=TTL
GBLoadWave/O/B/T={4,4}/w=1 /n=prefast
GBLoadWave/O/B/T={4,4}/w=1 /n=signal1wave
GBLoadWave/O/B/T={4,4}/w=1 /n=SHG
end
unction segmentation(TTL0,prefast0,signal1wave0,SHG0,pixsize)
wave TTL0
wave prefast0
wave signal1wave0
wave SHG0
variable pixsize
variable Nwave = dimsize(signal1wave0,0)
variable Sqpix = pixsize*pixsize
variable offset = 17 //The delay of the GV scanner
make/n=(Nwave) /o fast0
fast0[*] = prefast0[p+offset]

variable samplingnumber=210016
variable Nimage=(dimsize(TTL0,0)/samplingnumber)

make/n=(Nimage)/o TTLrising
make/n=(Nimage)/o TTLfalling
variable i
```

```
for(i=0;i<(Nimage);i+=1)
Findlevel /Q/Edge=1R=(i*samplingnumber,((i+1)*samplingnumber)-1)ttl0, 1
TTLrising[i]= round(V_Levelx)
Findlevel /Q/Edge=1R=(round(V_Levelx),((i+1)*samplingnumber)-1)/Edge2 ttl0, 1
TTLfalling[i]=round(V_Levelx)
endfor

make/0/n=(dimsize(TTLfalling,0)/d St
make/0/n=(dimsize(TTLfalling,0)/d Ed

St[][] = round(TTLrising[p])
Ed[][] = roiund(TTLfalling[p])
Matrixtranspose St
Matrixtranspose Ed

make/n=(pixsize*pixsize,(dimsize(TTLfalling,0)))/d/o fastave
make/n=(pixsize*pixsize,(dimsize(TTLfalling,0)))/d/o signal1ave
make/n=(pixsize*pixsize,(dimsize(TTLfalling,0)))/d/o SHGave

MultiThread fastave[][]=faverage(fast0,St[0][q]+p*(Ed[0][q]-
St[0][q]+1)/(pixsize*pixsize),St[0][q]+(p+1)*(Ed[0][q]-St[0][q}+1)/(pixsize*pixsize)-1)
MultiThread signal1ave[][]=faverage(signal1wave0,St[0][q]+p*(Ed[0][q]-
St[0][q]+1)/(pixsize*pixsize),St[0][q]+(p+1)*(Ed[0][q]-St[0][q]+1)/(pixsize*pixsize)-1)
MultiThread SHGave[][]=(-1)*faverage(SHG0,St[0][q]+p*(Ed[0][q]-
St[0][q]+1)/(pixsize*pixsize),St[0][q]+(p+1)*(Ed[0][q]-St[0][q]+1)/(pixsize*pixsize)-1)

make/n=(pixsize*pixsize,Nimage,3)/d/o preFWM3d
make/n=(pixsize*pixsize,3,Nimage)/d/o FWM3d

make/n=(pixsize*pixsize,Nimage,3)/d/o preSHG3d
```

```
make/n=(pixsize*pixsize,3,Nimage)/d/o SHG3d
variable scanrange
scanrange = 50 //[micrometer]

MultiThread preFWM3d[][][0]=p*scanrange/pixsize/pixsize
MultiThread preFWM3d[][][1]=fastave[p][q]*125
MultiThread preFWM3d[][][2]=signal1ave[p][q]
MultiThread FWM3d=preFWM3D[p][q][r]

MultiThread preSHG3d[][][0]=p*scanrange/pixsize/pixsize
MultiThread preSHG3d[][][1]=fastave[p][q]*125
MultiThread preSHG3d[][][2]=SHGave[p][q]
MultiThread SHG3d=preSHG3d3D[p][q][r]

Make/d/o/n=(pixsize*pixsize,3) triplet
Make/d/o/n=(pixsize*pixsize,3) tripletSHG
Make/d/o/n=(pixsize*pixsize,Nimage) interpolatedFWMimages
Make/d/o/n=(pixsize*pixsize,Nimage) interpolatedSHGimages

for(i=0;i<(Nimage);i+=1)
triplet = FWM3d[p][q][i]
imageinterpolate/S={0,scanrange/pixsize,scanrange,-
scanrange/2,scanrange/pixsize,scanrange/2}/dest+image_FWM Voronoi, triplet
STRING FWMdest = "The adress of the distination folder:"+"FWM"+num2str(i)+"tif"
imagesave /U/DS=32 image_FWM as FWMdest

tripletSGF = SHG3d[p][q][i]
imageinterpolate/S={0,scanrange/pixsize,scanrange,-
scanrange/2,scanrange/pixsize,scanrange/2}/dest+image_FWM Voronoi, tripletSHG
STRING SHGdest = "The adress of the distination folder:"+"SHG"+num2str(i)+"tif"
```

```
imagesave /U/DS=32 image_SHG as SHGdest
endfor

end

function TwoDimensionalPlots(pixsize)
variable pixsize
variable sqpix=(pixsize*pixsize)

autoloadwave()
wave TTL0
wave prefast0
wave signal1wave0
wave shg0
segmentation(TTL0,prefast0,signal1wave0,SHG0,pixsize)

wave image_FWM

end
```

Appendix. 2. Multiphoton imaging

I adopted the raster-scan configuration rather than a wide-field or light-sheet illumination scheme for the multi-photon imaging flow cytometer because the efficiencies of SHG and FWM is improved under stronger light fields by virtue of their nonlinear processes as described in section 2-1 and 2-2. The label-free imaging flow cytometer collects SHG and FWM signal from target cells simultaneously using multiple wavelength filters. In the SHG process, strong light fields interact with samples and induces second order optical polarization, generating a new photon with double energy (double frequency). In contrast, the FWM signal is spectrally broadened from the fundamental beam, and spectrally blue-shifted FWM signals are selectively detected with a long-pass filter located before the sample and a short-pass filter located after the sample.

Acknowledgements

First, I would like to express my gratitude to Professor Keisuke Goda for giving me the excellent opportunity to conduct optics research in his laboratory, including the development of a high-speed CARS imaging system, a pulse-shaping system using a spatial light modulator (SLM), and the label-free multiphoton imaging flow cytometer described in this thesis. Prof. Goda supervised my research and gave me the big picture of my research through monthly meetings. He also gave me valuable advice on how to improve my presentation slides, hold the microphone to tell my voice effectively, and handle Q&A sessions in the Research Seminar and Journal Club at the Weekly Meeting. As a result of this training, I received the Research Promotion Award for my master's program. In addition, I would like to thank him for giving me the valuable opportunity to launch the UTokyo SPIE student chapter and to work as its president. The outreach events, as well as the interaction with other universities' SPIE and OSA student chapters led to strengthen network among young optics researchers.

I would also like to thank my team leader, Assistant Professor Kotaro Hiramatsu, for all his help and support. During the weekly progress presentations in the Hiramatsu team, the active discussions regarding nonlinear optics, as well as the advice on troubleshooting that I encountered while working on my research, were beneficial for me to proceed with my doctoral research. In addition, the team's weekly reading sessions of papers and optics textbooks helped us to build up knowledge of related research.

I would also like to thank the secretaries and the office staff. Thanks to their support, I could smoothly carry out my daily research activities, including managing the purchase of items with my research grant.

Moreover, the daily communication in English with other members of Goda-lab, both in everyday conversation and research discussions, has obviously improved my English communication skills. It was also a valuable experience to be exposed to various background cultures in the global environment of Goda-Lab with high diversity. When I entered the University of Tokyo, the President of the University of Tokyo, Junichi Hamada, told a slogan, "Be a tough and global student at the University of Tokyo." My research life in Goda-lab, from undergraduate to Ph.D. course, has provided me with essential elements to be a "tough and global" researcher. I will continue my life as a researcher with this valuable experience in Goda-lab.

Finally, I would like to express my gratitude to JSPS (DC1) for supporting the research fund and living expenses during my doctoral program.

Publications list

1. Kinegawa, R., Gala de Pablo, J., Wang, Y., Hiramatsu, K., & Goda, K. Label-free multiphoton imaging flow cytometry. *Cytometry Part A*, 103, 584-592 (2023).

2. Lindley, M., Gala de Pablo, J., Kinegawa, R., Hiramatsu, K., & Goda, K. Highly sensitive Fourier-transform coherent anti-Stokes Raman scattering spectroscopy via genetic algorithm pulse shaping. *Optics Letters*, 46, 4320-4323 (2021).

3. Kinegawa, R., Hiramatsu, K., Hashimoto, K., Badarla, V. R., Ideguchi, T., & Goda, K. High-speed broadband Fourier-transform coherent anti-Stokes Raman scattering spectral microscopy. *Journal of Raman Spectroscopy*, 50, 1141-1146 (2019).